Institute for Geophysics, Astrophysics, and Meteorology
University of Graz

Atmospheric Remote Sensing and Climate System Research Group
ARSCliSys - on the art of understanding the climate system

IGAM/UniGraz Technical Report for ESA/ESTEC No. 1/2005

ESA study:

ACEPASS — LEO–LEO Occultation Characterisation Study
[ESA/ESTEC Contract No. 16743/02/NL/FF, ACEPASS CCN-3 Study Part]

Advanced Wave-Optics Processing of LEO-LEO Radio Occultation Data in Presence of Turbulence

by

Michael E. Gorbunov[1,2] and Gottfried Kirchengast[2]

[1] Institute of Atmospheric Physics, Moscow, Russia
[2] IGAM, University of Graz, Graz, Austria

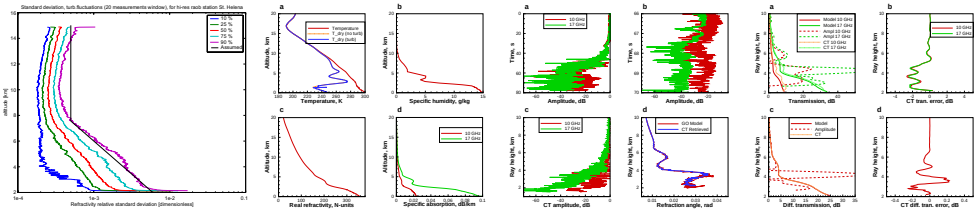

March 2005

Advanced Wave-Optics Processing of LEO-LEO Radio Occultation Data in Presence of Turbulence

M. E. Gorbunov[1,2] and G. Kirchengast[2]

[1] Institute of Atmospheric Physics, Moscow, Russia
[2] IGAM, University of Graz, Graz, Austria

Abstract

Canonical Transform (CT) and Full-Spectrum Inversion (FSI) methods can be used to retrieve integral absorption, or transmission, profiles from radio occultation (RO) data. Transmission data are necessary, in addition to bending angles, for the retrieval of atmospheric humidity without using auxiliary measurements. LEO-LEO occultations using X/K-band frequencies within 9–23 GHz, such as planned for the Atmosphere and Climate Explorer mission ACE+, can provide the transmission data along the wing of the 22 GHz water vapor absorption line. The computation of integral absorption from the amplitude of the wave field requires spherical symmetry of the atmospheric refractivity. This condition is broken in presence of turbulence, which can result in significant errors in the retrieved transmission. Using ACE+ frequencies as baseline (such as 10 and 17 GHz), we discuss CT/FSI retrieval techniques, with the differential method applied to correct for the effect of turbulence. We suggest the computation of the differential transmission from the differential CT/FSI-amplitude of the wave field in the transformed pace. The method uses the fact that the amplitude of the wave field in the representation of the impact parameter is independent from frequency in the asymptotic approximation. The efficiency of the method was tested by numerical end-to-end simulations at very high forward modeling resolution (∼200 m horizontally, ∼1 m vertically). We modeled turbulence as 2D random field perturbations in the occultation plane of refractivity background fields from smooth analytical models, high-resolution radiosondes, and ECMWF analysis fields. Turbulence modeling was done based on Gaussian and Power forms of the spectrum, the latter being the most realistic model. Turbulence cases were included with the magnitude of turbulent fluctuations estimated from high resolution radiosondes at both low and high latitudes. The simulations demonstrate that the error in the retrieved transmission can be significant in the lower-to-mid troposphere in a single frequency channel, while the differential transmission can be retrieved with high accuracy down towards the boundary layer. The Conclusions and Outlook section provides a range of specific conclusions.

1 Introduction

Radio occultations using GPS signals proved to be a very powerful technique of sounding the Earth's atmosphere [*Kursinski et al.*, 2000]. However, atmospheric refractivity indicates very weak absorption and dispersion at GPS frequencies. This makes it impossible to separate the dry and wet terms of the retrieved refractivity without employing additional a priori information. Use of an observation system of Low Earth Orbiters (LEOs) implemented with transmitters and receivers of radio signals in 9–30 GHz band can solve this problem [*Kursinski et al.*, 2002; *Kirchengast et al.*, 2004b, a]. Water vapor has an absorption line centered near 22 GHz. Therefore, from measurements of phase and amplitude, complex refractive index can be retrieved. Then, pressure, temperature, and water vapor profiles can be solved for, using a spectroscopic model of the water vapor line and the hydrostatic equation. [*Kirchengast et al.*, 2004a] describe this retrieval processing in detail, but restricted to the geometric-optics approach for the transmission and bending angle retrieval.

Here the focus is on transmission and bending angle retrieval by wave-optical methods, which will be the approach generally required with real data, since the retrieval scheme will encounter a significant challenge in case of turbulence. The amplitude of a radio occultation signal is significantly more sensitive to small scale turbulence than the phase [*Yakovlev et al.*, 1995; *Sokolovskiy*, 2001]. In presence of small scale structures and turbulence, the amplitude of the wave field undergoes strong scintillations, which can overwhelm the effect of absorption. In order to reduce the effect of scintillations due to diffraction and multipath, it was suggested to use twin frequencies [*Kursinski et al.*, 2002]. Similarly, it was suggested for scintillations due to isotropic turbulence to use closely spaced twin frequencies for effect reduction [*Facheris and Cuccoli*, 2003].

Given the measurements of the wave field $u_1(t)$ and $u_2(t)$ for two frequencies f_1 and f_2, the difference $\Delta f = f_1 - f_2$ being small enough, we consider the ratio $|u_1(t)| \,/\, |u_2(t)|$. Because for neighbor frequencies the effects of diffraction and interference will not differ significantly, it is expected that they will be reduced in the ratio. The amplitude is proportional to the absorption factor $\exp(-\tau_{1,2})$, where $\tau_{1,2}$ is the integral absorption along a ray for frequency f_1 or f_2. In this case $\ln(u_1(t)/u_2(t))$ equals differential absorption, $\tau_2 - \tau_1$. However, this is only valid for Δf being small enough. On the other hand, choice of too small Δf will result in too low values of the differential absorption, which will increase the noise sensitivity.

The wave optics processing methods such as Canonical Transform (CT) [*Gorbunov*, 2002a; *Gorbunov and Lauritsen*, 2002; *Gorbunov et al.*, 2004;

Gorbunov and Lauritsen, 2004] or Full-Spectrum Inversion (FSI) [*Jensen et al.*, 2003, 2004] are based on the transform of the wave field into the representation of impact parameter. In this representation, the derivative of the phase of the transformed wave field is a function of refraction angle, and the amplitude describes the distribution of the energy with respect to impact parameters. For a spherically-symmetric atmosphere, the amplitude of the transformed wave field is proportional to the exponential function of the integral absorption along the ray. Therefore, CT and FSI techniques can be used for the retrieval of atmospheric absorption [*Gorbunov*, 2002b; *Jensen et al.*, 2004]. These techniques will significantly reduce retrieval errors due to multipath and diffraction. However, the problem of turbulence still persists. Because turbulence is a 3D inhomogeneous structure, the amplitude of the transformed wave field also indicates scintillations [*Sokolovskiy*, 2001].

In this study, we suggest using the differential method as the method of retrieval of absorption in combination with CT or FSI technique. The wave field $u_{1,2}(t)$ is first processed by the Fourier Integral operator (FIO) $\hat{\Phi}$, defined in the CT and FSI methods. The transformed wave field $\hat{\Phi}u_{1,2}(p)$ at each single frequency is then to a very significant extent free from the effects of diffraction and multipath. These effects may only be significant for small scale atmospheric inhomogeneities, with scales below 50 m [*Gorbunov et al.*, 2004]. The logarithmic ratio of the transformed amplitudes $\ln\left(\left|\hat{\Phi}u_1(p)\right| / \left|\hat{\Phi}u_2(p)\right|\right)$ will then further suppress the scintillations due to small scale turbulence and will be equal to the differential absorption $\tau_2 - \tau_1$ with a much higher accuracy then the direct amplitude ratio $\ln(|u_1(t)| \,/\, |u_2(t)|)$.

We tested the performance of this new type of differential method in numerical simulations. In the simulations we used different models of the atmosphere: 1) 3D global fields from an ECMWF analysis without superposition of turbulence (smoothly variable fields, for reference), 2) high-resolution radio sonde profiles (highly vertically structured fields, but spherically-symmetric in the horizontal), 3) smooth analytical background atmosphere profiles with superposition of random 2D turbulence, 4) 3D ECMWF analysis field with superposition of random 2D turbulence with magnitudes estimated from high-resolution radiosonde data. The simulations include investigation of the sensitivity of the method to thermal noise in the receiver with a realistic noise level and to amplitude drifts (using the ACE+ baseline values C/N_0 of 67 dBHz, drifts of 0.5% over 20 sec).

2 Description of Method

Given measurements of the complex wave field during a radio occultation experiment, $u(t)$, its transform to the representation of the impact parameter is given by the following FIO:

$$\hat{\Phi}u = \sqrt{\frac{-ik}{2\pi}} \int a(p,Y) \exp(ikS(p,Y))u(Y(t))dY, \tag{1}$$

where $k = \dfrac{2\pi}{\lambda}$ is the wavenumber, $a(p,Y)$ and $S(p,Y)$ are the amplitude and phase function of the FIO, respectively, Y is a convenient coordinate along the trajectory:

$$dY = d\theta - \frac{dr_T}{r_T}\frac{p_0}{\sqrt{r_T^2 - p_0^2}} - \frac{dr_R}{r_R}\frac{p_0}{\sqrt{r_R^2 - p_0^2}} \tag{2}$$

where r_T and r_R are (LEO-)Transmitter and (LEO-)Receiver satellite radii, and θ is the the angular distance between the satellites in the coordinate system of the local curvature center. Coordinate Y generalizes the use of coordinate θ in the FSI method [*Jensen et al.*, 2003]. Explicit expressions for the amplitude and phase functions involving satellite orbit data were recently derived by [*Gorbunov and Lauritsen*, 2002; *Jensen et al.*, 2004; *Gorbunov and Lauritsen*, 2004]. In particular the amplitude function has the following form:

$$a(p,Y) = \left(\sqrt{r_R^2 - p^2}\sqrt{r_T^2 - p^2}\frac{r_R r_T}{p}\sin\theta\right)^{1/2}, \tag{3}$$

As shown by *Gorbunov and Lauritsen* [2004], the asymptotic solution of the wave propagation can be expressed in terms of the inverse FIO with the following amplitude function:

$$a^*(Y,p) = \left(\frac{1}{\sqrt{r_R^2 - p_R^2}\sqrt{r_T^2 - p_T^2}}\frac{p_T}{r_R r_T \sin\theta}\frac{dp_T}{dp}\right)^{1/2}, \tag{4}$$

where p_T and p_R are the impact parameters at transmitter and receiver satellite, and p is the effective impact parameter, computed from the Doppler frequency shift using the formula of Bouguer [*Vorob'ev and Krasil'nikova*, 1994]. For a spherically symmetric atmosphere, $p_R = p_T = p$.

Generally, due to horizontal gradients, these three impact parameters are different, and the following equation can be established [*Gorbunov and Kornblueh*, 2001]:

$$p_R = p_T + \int \frac{\partial n}{\partial \theta} ds, \tag{5}$$

where the integral is taken along the ray. Impact parameter is computed from the Doppler frequency, or optical path derivative, $\dot{\Psi} = \mathbf{V}_R\mathbf{u}_R - \mathbf{V}_T\mathbf{u}_T$, where $\mathbf{V}_{R,T}$ are the satellites velocities and $\mathbf{u}_{R,T}$ are the unit vectors of the rays at the receiver and transmitter. This expression can be rewritten as a sum of radial and angular component. From the orbital data, we can find radii $r_{R,T}(t)$ and polar angles $\theta_{R,T}(t)$ of the satellites in some occultation plane, as well as the angular separation $\theta(t) = \theta_R(t) - \theta_T(t)$. This allows to write:

$$\dot{\Psi} = \dot{\theta}_R r_R \sin\psi_R - \dot{\theta}_T r_T \sin\psi_T + \dot{r}_R \cos\psi_R + \dot{r}_T \cos\psi_T = \\ = \dot{\theta}_R p_R - \dot{\theta}_T p_T + \frac{\dot{r}_R}{r_R}\sqrt{r_R^2 - p_R^2} + \frac{\dot{r}_T}{r_T}\sqrt{r_T^2 - p_T^2}. \quad (6)$$

For a spherically symmetric medium we have the following relation:

$$\dot{\Psi} = \dot{\theta}p + \frac{\dot{r}_R}{r_R}\sqrt{r_R^2 - p^2} + \frac{\dot{r}_T}{r_T}\sqrt{r_T^2 - p^2}. \quad (7)$$

For a 3D medium these equations are used for the computation of effective impact parameter and bending angle that can be used in 3D-Var/4D-Var schemes, for example [*Gorbunov and Kornblueh*, 2001], or as basis for subsequent retrieval. Equations (5,6,7) allow to express p_R and p_T as functions of effective impact parameter p. The relation between p, p_R, and p_T includes the horizontal gradient of refractive index $\dfrac{\partial n}{\partial \theta}$, however, which is unknown a priori.

Proceeding further, the amplitude of the transformed wave field retrieved by the CT or FSI method will then be equal to the following expression:

$$A_{1,2}(p) = \bar{A}_{1,2}\frac{\sqrt{r_R^2 - p^2}\sqrt{r_T^2 - p^2}}{\sqrt{r_R^2 - p_R^2}\sqrt{r_T^2 - p_T^2}}\frac{p_T}{p}\frac{dp_T}{dp}\exp(-\tau_{1,2}(p)) \equiv \\ \equiv \bar{A}_{1,2}K(p)\exp(-\tau_{1,2}(p)), \quad (8)$$

where $\bar{A}_{1,2}$ are some normalizing constants (which are, generally speaking, different for different channels). This expression can be represented as a composition of the normalizing constant $\bar{A}_{1,2}$, integral absorption along the ray $\exp(-\tau_{1,2}(p))$, and the factor $K(p)$ that depends on the horizontal gradients. For a spherically layered medium, where $p_R = p_T = p$, factor $K(p)$ equals unity. In this case the absorption can be retrieved from the CT amplitude:

$$\tau_{1,2}(p) = \ln\left(\bar{A}_{1,2}/A_{1,2}(p)\right) \quad (9)$$

For a 3D medium with horizontal gradients, factor $K(p)$ approximately equals $\frac{dp_T}{dp}$, differing from unity. This shows that in presence of 3D inhomogeneities, in particular, atmospheric turbulence, the amplitude of the transformed wave field, $A_{1,2}(p)$ will undergo scintillations. Because factor $K(p)$ is unknown a priori, this will lead to error of the retrieval of the absorption in each channel. The error will be of magnitude $\ln K(p)$.

It is important to observe that $K(p)$ does not depend on the frequency of the wave field, i.e., it is the same for all frequency channels. This frequency-independency roots in the non-dispersive character of the refractive index in the wavelength domain of interest, which implies that optical paths are the same at different frequencies for any refractivity field, whether smooth or randomly varying. Thus the term $\ln K(p)$ will cancel in the differential transmission $\tau_2(p) - \tau_1(p)$ and only some residual diffractive effects not captured by the CT-plus-ratioing formulation will be left. These residual errors are best assessed by numerical simulations as discussed below. The normalizing constants $\bar{A}_{1,2}$ can be estimated in the standard way by the analysis of the wave field at heights 25-30 km. Then the logarithmic ratio of the normalized amplitudes will be expressed as follows:

$$\ln \frac{A_1(p)/\bar{A}_1}{A_2(p)/\bar{A}_2} = \tau_2(p) - \tau_1(p). \tag{10}$$

Here transmissions $\exp(-\tau_{1,2}(p))$ are measured in Neper. Multiplication with a factor of $20/\ln 10$ will convert them to dB.

The described method is assessed and verified below by rigorous wave optical forward-inverse simulations including a variety of cases ranging from smoothly varying refractivity fields to fields containing severe small-scale random turbulence and thermal receiver noise.

3 Numerical Simulations

3.1 Simulations with ECMWF 3D fields without turbulence

In order to illustrate the capability of the differential method to handle horizontal gradients, we performed simulations with a smoothly varying 3D model of refractive index (no variation at turbulent scales). We used global fields of temperature, pressure, and specific humidity from an analysis of the European Centre for Medium Range Weather Forecasts (ECMWF). Figure 1 shows the local profiles of the atmospheric constituents at the tangent point

location of the occultation. Shown are temperature T, dry temperature $T_{\rm dry}$ (including the effect of humidity), specific humidity q, real refractivity N, and specific absorption $(20/\ln 10)kN_I$, which is proportional to imaginary refractivity N_I, and $(20/\ln 10)$ is the Neper-to-dB conversion factor.

The forward simulation was based on the multiple phase screen technique [*Martin*, 1992; *Gorbunov and Gurvich*, 1998]. The integration step between screens was 10 km. Figure 2 shows the results of the simulation and the CT inversion. Shown are amplitudes for the two channels as functions of time, CT amplitude and bending angles as function of the ray impact height, which is defined as $p - r_E$, where r_E is the local curvature radius of the reference ellipsoid. We present the bending angle profile computed by the geometric-optics forward modeling and compare it with the bending angle profile retrieved from the simulated occultation data by the CT method. Both bending angle profiles are in very good agreement. The plot of the amplitude reveals two multipath regions associated with the two spikes of the bending angle profile, near 4 and 2.5 km. The amplitude record in multipath regions indicates strong interference oscillations. Enlarged interference patterns are shown separately, in panel (b), for a 4 sec sub-interval. This panel illustrates the difference of the interference patterns in the two channels in multipath areas.

Figure 3 shows the results of the computation of transmission. In panel (a) we show true transmissions, transmissions computed directly from the amplitude of the measured wave field, $|u_{1,2}(t)|$, and transmissions computed from the CT amplitude, respectively. The computation of the transmissions directly from the measured amplitude $|u_{1,2}(t)|$ uses the following expression for the amplitude of a radio occultation signal under the assumption of sphericity and single-ray propagation [*Jensen et al.*, 2004; *Gorbunov and Lauritsen*, 2004]:

$$|u_{1,2}(t)| = \left\{ \frac{1}{\sqrt{r_T^2 - p^2}\sqrt{r_R^2 - p^2}} \left[1 - \frac{p}{r_T\sqrt{r_T^2 - p^2}} \frac{dr_T}{d\theta} - \right.\right.$$
$$\left.\left. - \frac{p}{r_R\sqrt{r_R^2 - p^2}} \frac{dr_R}{d\theta} \right]^{-1} \frac{p}{r_T r_R \sin\theta} \frac{dp}{d\theta} \right\}^{1/2} \exp(-\tau_{1,2}(p)). \quad (11)$$

Here impact parameter is assumed to be a single-valued function of time, computed from the Doppler frequency [*Vorob'ev and Krasil'nikova*, 1994]. The errors of the retrieval of transmission from the measured amplitude significantly exceed the errors of CT transmission. Panel (b) shows that the errors of CT transmission are very close to each other except the region below

the ray height of 2.5 km. This indicates that above 2.5 km the main source of the transmission retrieval error is horizontal inhomogeneities. Below 2.5 km, the absorption in the second channel (20 GHz) is very strong, which results in too weak a signal. Here the numerical noise becomes a main error source. Note that in this example, the ray impact height of approximately 2 km corresponds to the 0 km altitude (ground level) of the tangent point, i.e., below 2.5 km impact height no accurate results could be expected in reality anyway.

Panel (c) of Figure 3 presents the differential transmissions: true one, differential transmissions computed directly from the measured amplitudes, and CT differential transmissions. Errors of the latter are shown in panel (d). Above 5 km, the errors are very low, of order of 0.001 dB. These errors are due to the initialization. We assume that above 25 km absorption is zero and compute the normalizing constants $\bar{A}_{1,2}$ by averaging the amplitudes $A_{1,2}(p)$ over the ray height interval 25–30 km. The Liebe model predicts a small transmission of about 5×10^{-3} dB and a differential transmission of about 10^{-3} dB for these heights. This results in the constant systematic error of the retrieved transmission, which will not propagate into imaginary refractivity in subsequent processing, however, since this retrieval depends on the derivative of transmission only [*Kursinski et al.*, 2002; *Kirchengast et al.*, 2004a]. The relative error (not shown) increases with height, as absorption decreases, and reaches about 100% beyond 20 km (cf. the detailed discussion of [*Kirchengast et al.*, 2004b, a]). Below 5 km, the errors increase to 0.1-0.2 dB (2-5%). Below 2.5 km (close to ground as explained above), the signal in the 20 GHz channel becomes very weak (strongly attenuated) and the errors increase sharply.

Note that in this case and all following cases, the transmissions shown are filtered to a height resolution of ∼1 km, in line with the vertical resolution requirement for ACE+ [*ESA*, 2004]. The (differential) transmission accuracies are thus those at 1 km height resolution, conistent with the resolution utilized for the geometric-optics performance results such as shown in [*Kirchengast et al.*, 2004b; *ESA*, 2004].

3.2 Simulations with high resolution radiosonde data

Figures 4, 5, and 6 show results of a simulation with high-resolution radio sonde data. The profiles contain small scale structures with a characteristic vertical scale of a few 10 meters only. The profile was used to generate a spherically symmetric atmosphere, which evidently contains layered inhomogeneities with strong vertical refractivity gradients. At a ray height of 3 km we observe a sharp spike of refraction angle, which is characteristic for a

super-refraction layer. We modeled radio occultation data using multiple the phase screen technique, the integration step between screens being 1 km. In this simulation, there are no horizontal gradients, and the main error source is the diffraction due to thin spherical layers.

From the geometric-optics view point, many of the layers can form wave guides. Rays from outside of the atmosphere, approaching from the transmitter, cannot have perigee points inside the layers. In wave optics, though, energy can propagate into such layers and create modes corresponding to geometric optical rays confined in the wave guide. This is observe for the ray with an impact height of about 3 km. This ray has a big interaction length with the super-refraction layer, and a part of its energy propagates into the layer. Due to that the CT amplitude indicates a drop near a ray height of 3 km. Because effects of diffraction depend on frequency, the errors of the transmissions at 9 and 17 GHz are not as well correlated as in the previous example. On the other hand, below about 5 km ray height (below about 3 km altitude), the errors due to diffraction are significantly smaller than those due to horizontal gradients. The differential transmission is retrieved with an accuracy of 1-2%.

Figure 7 shows the results of a simulation for closely-spaced twin frequencies at 17 and 17.3 GHz, a case similar to the ones studied by [*Facheris and Cuccoli*, 2003] and subsequent work of these authors. This simulation shows that the use of closely spaced twin frequencies results in the increase of the errors of the retrieved transmissions. The accuracy of CT differential transmission is 2-5%. This can be explained as follows. For twin frequencies, 17 and 17.3 GHz, the correlation of errors due to diffraction are better than for 9 and 17 GHz. However, the differential transmission itself is also significantly smaller due to the close spacing of the frequencies. It was expected that the ratio of directly measured amplitudes will give a good estimation of the differential transmission. However, in this example we see that, due to multipath propagation, the standard method of retrieval of the differential transmission from the ratio of measured amplitudes results in significant errors. The accuracy of the CT technique is much better. This indicates that wave-optics processing of amplitudes to the transformed space will be a standard pre-processing step in the processing of real X/K band absorptive occultation data.

3.3 Simulations with turbulence models and random thermal noise

Simulations with horizontally-inhomogeneous turbulence are crucial for the assessment of the performance of the method discussed. We investigated somewhat an-isotropic turbulence — as fully isotropic one is computationally prohibitive in our explicit turbulence modeling approach — with different forms of the turbulence power spectrum $\tilde{B}(\kappa)$, where $\kappa = \left(\kappa_z^2 + q^2 \frac{\kappa_\theta^2}{r_E^2}\right)^{1/2}$, κ_z and κ_θ are the spatial frequencies (wavenumbers) conjugated to the polar coordinates z and θ in the occultation plane, q is the anisotropy coefficient set to values of 10 to 100. For each turbulence case, a random realization of a 2D cross-section of the turbulence field $\tilde{B}(\kappa) = \tilde{B}(\kappa_z, \kappa_\theta)$ was computed. $f(z, \theta)$ was understood as the relative perturbation of refractivity due to the turbulence. The refractive index field was then computed as $1 + N(z, \theta)\,(1 + f(z, \theta))$, where $N(z, \theta) = n(z, \theta) - 1$ is the regular (non-random background) model of refractivity. The simulations were performed by means of the multiple phase screen technique at very high resolution (200-500 m horizontal, about 1 m vertical).

The simpler not tremendously realistic turbulence model used was based on the Gaussian form of $\tilde{B}(\kappa)$:

$$\tilde{B}(\kappa) = c \exp\left[-\frac{(\kappa \Delta z)^2}{2}\right], \tag{12}$$

where c is the normalizing constant. For the severe-turbulence demonstration case discussed first below, it was chosen in such a way that $\langle f(z, \theta)^2 \rangle^{1/2} = 0.01$. The anisotropy coefficient q was taken to equal 100, and the vertical turbulence scale $\Delta z = 0.2$ km.

The regular refractivity field was computed for the following temperature and specific humidity profiles:

$$T(z) = T_0 + \Delta T \cos\left(\frac{2\pi z}{\Delta z_T}\right), \tag{13}$$

$$q(z) = q_0^{(h)} \exp\left(-\frac{z}{\Delta h}\right) + q_0^{(l)} \exp\left(-\frac{\left(z - z_0^{(l)}\right)^2}{\Delta l^2}\right), \tag{14}$$

where we set $T_0 = 250$ K, $\Delta T = 20$ K, $\Delta z_T = 30$ km, $q_0^{(h)} = 0.015$ kg/kg, $\Delta h = 3$ km, $q_0^{(l)} = 0.010$ kg/kg, $z_0^{(l)} = 3$ km, $\Delta l = 1$ km.

Figure 8 shows the regular profiles of the temperature T, and dry temperature $T_{\rm dry}$, specific humidity q, refractivity N, and specific absorption $(20/\ln 10)kN_I$. The rms turbulence fluctuations of local temperature are estimated as $T\left\langle f(z,\theta)^2\right\rangle^{1/2} \approx 3$ K, an extreme case. In panel (a) we plot, as an illustration, turbulent dry temperature $T_{\rm dry}^{\rm (turb)}$ computed for the retrieved refractive index. It is found that the rms turbulent perturbation of retrieved $T_{\rm dry}$ is near 1 K, which is less than the above estimation of the fluctuations of local temperature, 3 K. This is explained by the fact that we are looking at retrievals, refractivity is retrieved from bending angles, which depend on turbulent fluctuations averaged along rays.

Figures 9 and 10 show the results of modeling with turbulence with the Gaussian spectrum; these have been computed for 10 and 17 GHz frequency channels. The integration step between the phase screens was taken 0.5 km. The CT amplitudes for the two channels indicate very similar perturbations due to horizontal inhomogeneity. The effect of horizontal gradients manifests itself in the bending angles computed by the GO model. Below 3.5 km impact height, the GO refraction angle profile is multi-valued due to the strong perturbations of the impact parameters.

Figure 10 presents the results of the retrieval of transmission. Strong multipath propagation takes place for ray heights below 5.5 km. Here, the transmission retrieved from the measured amplitudes has significant errors as shown in panel (a). CT transmission errors, plotted in panel (b), are less significant and they are well correlated for the two frequencies. The differential transmission directly from the measured amplitudes has significant errors, 10–20 dB below 5.5 km. The CT differential transmission is in a good agreement with the true one. The retrieval errors are less than 3% above about 4 km impact height.

Furthermore, a more realistic turbulence model of power form was adopted:

$$\tilde{B}(\kappa) = \begin{cases} c\kappa_{ext}^{-\mu},\ \kappa < \kappa_{ext} \\ c\kappa^{-\mu},\ \kappa_{ext} \le \kappa \le \kappa_{int} \\ c\kappa^{-\mu} \exp\left[-\left(\dfrac{\kappa - \kappa_{int}}{\kappa_{int}/4} \right)^2 \right],\ \kappa > \kappa_{int} \end{cases}, \qquad (15)$$

where κ_{ext} is the wavenumber of the external scale of the sub-range of turbulence, κ_{int} is the one of internal scale, and μ is the power of the spectrum.

Figures 11 and 12 present the results of a simulation example with external scale $2\pi/\kappa_{ext} = 1$ km, internal scale $2\pi/\kappa_{int} = 0.03$ km, exponent $\mu = -4$ (which corresponds to -5 for 3D spectrum), and anisotropy $q = 20$. This form of spectrum and the parameters chosen provide a realistic spectrum for the free atmosphere (above the atmospheric boundary layer) according

to theoretical and experimental studies [*Fritts et al.*, 1988; *Fritts and VanZandt*, 1993; *Fritts and Alexander*, 2003; *Gurvich and Brekhovskikh*, 2001; *Gurvich and Chunchuzov*, 2003, 2005]. The normalizing constant c was chosen in such a way that the magnitude of the relative turbulent perturbation equals 0.005, which corresponds to turbulent perturbations of temperature of about 1.5 K, again a very strong case.

Note that the adopted internal scale of 30 m exceeds the real internal scale, which is of order 1 cm only. However, small scale inhomogeneities provide small input into amplitude fluctuations. According to [*Yakovlev et al.*, 2003; *Kan et al.*, 2002], the amplitude scintillation spectra for a wavelength of 2 cm (15 GHz) at scintillation frequencies > 20 Hz provide a very small contribution into the scintillation power, due to the steep spectral slope. For the characteristic vertical scan velocity of 1 km/s for LEO-LEO occultations in the troposphere, this frequency range with small contribution corresponds to inhomogeneities with vertical scales < 50 m.

Furthermore, from a complementary perspective, the modeled internal scale of 30 m approximately corresponds to the diffraction limit derived by *Gorbunov et al.* [2004]: $h \geq \sqrt[3]{2\lambda^2 r_E}$. This is the estimate of the smallest vertical scale of inhomogeneities, which play a significant role in diffraction/scintillation effects, i.e., inhomogeneities with smaller scales produce a very small input into amplitude scintillations. A detailed theoretical analysis of this behavior was given by *Rytov et al.* [1989] who analyzed the input of different spatial frequencies of turbulence into amplitude scintillations and showed that amplitude scintillation frequency is limited at the high-frequency end by diffraction effects.

For the ACE+ case with channels near 15 GHz, the diffractive limit is about 20 m. In the present study we have chosen 30 m in our numerical simulations, as close as possible to this limit; the difficulties and computational demand for numerical simulations of turbulence in an explicit random field modeling approach increase dramatically with modeling smaller vertical scales. However, while we do not expect significant changes in the results, we might attempt simulations with scales down to 10 m based on further modeling developments, and even faster computers, in the future.

Regarding the choice of anisotropic turbulence, it was shown by *Kan et al.* [2002]; *Gurvich* [1984, 1989]; *Gurvich and Brekhovskikh* [2001] that the main input into scintillation above the atmospheric boundary layer (> 2 km) comes from anisotropic turbulence. For example, *Gurvich and Brekhovskikh* [2001] analyzed the dependence of the scintillation amplitude on the anisotropy coefficient q and found, backed by experimental data, that scintillations increase as q increases from 1 to about 10, then the effect is saturated. The

reason is that isotropic turbulence of a given vertical scale has, compared to anisotropic one, smaller correlation radius horizontally along-ray, wherefore the observed along-ray integrated scintillation effect is smaller. We may verify this in future simulations, again computationally very demanding, down to anisotropy coefficients as small as 5.

Panel (a) of Figure 11 shows that the power model of turbulence results in more severe amplitude scintillations than the simpler Gaussian turbulence model. Panel (b) shows that GO refraction angle profile has a very complicated small-scale structure (scales 30–50 m), which is not well reproduced by the CT retrieval. This can be attributed to the effects of diffraction. Figure 12 shows that the accuracy of the CT differential transmission based on the power turbulence model is still within 0.2 dB (accuracy better than 5%) down to an impact height of below 6 km (altitudes below 5 km) in this severe case. Simulations based on a larger high-resolution radio sonde database have been performed at University of Bremen (S. Buehler, private communications, 2004) in order to assess what typical rms refractivity fluctuations are to be expected in the real atmosphere, so as to put the levels of several 0.1% rms used here (0.5% in the present case) into perspective. Results based on simulating such realistic fluctuation levels are presented in the following section.

Figure 13 shows the results of modeling for the same model of the turbulent atmosphere with addition of modeling random noise in the receiver. We modeled a $R_{CN} = 67$ dBHz carrier-to-noise ratio above the atmosphere, consistent with the R_{CN} baseline assumption for ACE+. We used a sampling rate of $F_S = 1000$ Hz. Therefore, the noise-to-carrier ratio can be estimated as $10^{-R_{CN}/20}\sqrt{F_S/2} \approx 1\%$, or -40 dB. Figure 13 shows that the noise influence is only visible below an impact height of 5 km, where the transmission in the 17 GHz channel starts to exceed 20 dB, and, more importantly, the total attenuation (absorption and defocusing) is starting to strongly decrease the R_{CN}.

Test simulations with smaller R_{CN} (e.g., 64 dBHz) showed that in this case noise effects start to show up higher up, which confirms that the ACE+ 67 dBHz baseline, while not being derived taking the wave-optics 1 kHz sampling rate processing requirements directly into account, was selected just at the right level of stringency also for this purpose. Test simulations also confirmed that a 1 kHz sampling rate is the minimum sampling rate needed for the wave-optical processing in the X/K band. Furthermore, regarding small amplitude drifts of type 0.5% over 20 sec from 25 km downwards (another ACE+ specfication), tests showed that the effects of these is very small on the wave-optics processing performance, i.e., of minor relevance compared to thermal noise.

3.4 Simulations with ECMWF 3D fields, turbulence modeling, and thermal noise

A realistic model of the turbulent atmosphere includes the regular part from ECMWF analyses and small-scale turbulence with a magnitude chosen as estimated from high resolution radiosonde measurements. Figures 14 and 15 show the magnitude of turbulent fluctuations for different percentiles for a > 1 year dataset from a low-latitude and high-latitude station, respectively (S. Buehler, Univ. of Bremen, pers. communications, 2004); S. Buehler computed these by using the same radiosonde database and filtering method for isolating turbulent fluctuations as used in *Buehler* [2004] and then, rather than estimating C_n^2 values, estimating the rms values from the data in a range of ∼200 m about each height level.

Since the turbulent fluctuations estimated by *Buehler* [2004], analyzed in terms of C_n^2, compare reasonably well with those from S. Sterenborg and P. Baptista (ESA/ESTEC, Noordwijk, Netherlands, pers. communications, 2004) used as baseline for [*Kirchengast et al.*, 2004b] and the subsequent ACE+ Report for Mission Selection [*ESA*, 2004], the results below are based on comparable assumptions of turbulence as these earlier results. While *Kirchengast et al.* [2004b] used the simple parametric scintillation model by *Kuhn* [2003] assuming median (50% percentile) turbulence levels, we use here explicit turbulence modeling reflecting the upper decile (90% percentile) turbulence levels (see Figures 14 and 15). This means, assuming the rms estimates are reasonably correct, that about 90% of the ACE+ profiles will see less turbulence than modeled here at any given height.

Figures 16, 17, and 18 show the results of simulations for an ECMWF analysis field and power turbulence superposed. Here, we first modeled an occultation at low latitudes in the tropical region. The turbulence model has been set to external scale $2\pi/\kappa_{ext} = 0.3$ km, internal scale $2\pi/\kappa_{int} = 0.03$ km, exponent $\mu = -4$ (-5 for 3D spectrum), and anisotropy $q = 20$. The phase screen spacing was set to 200 m. The normalizing constant c is assumed to be a function of altitude z here. For this event, its choise was based on Figure 14. The magnitude of the relative turbulent perturbation equals 0.006 (0.6%) at a height of 2 km, and log-linearly decreases to 0.0005 (0.05%) at a height of 7.5 km. Beyound this interval, $c(z)$ is kept constant. This model corresponds to fairly strong turbulence with significant small-scale components.

The refraction angle profile is typical for the tropical region and it indicates strong multipath propagation. The random error of CT transmission is significant below about 6 km (> 0.3 dB), but the CT differential transmission is within 0.2 dB (4–5%) std.deviation down into the boundary layer and within 0.1 dB (∼2%) down to below 5 km ray height (below 4 km al-

titude). It is, furthermore, clearly evident from the top-left and bottom-left panels of Fig. 18 that direct use of amplitudes or direct use of amplitude ratios without CT exhibits grossly inferior performance in the lower to middle troposphere and leads to an error > 0.3 dB all over this domain. For perspective, in the atmospheric profiles retrieval algorithm used in *ESA* [2004], the so-called best-fit temperature extrapolation is generally activated at heights below which the transmission errors start to exceed 0.3 dB.

Figure 19 shows the results of processing the same simulated event with, in addition, superimposing receiver noise with a magnitude of 67 dBHz above atmosphere. Comparing to Figure 18 it can be seen that the receiver noise has insignificant effects above a ray height of about 4 km but is clearly relevant below about 3.5 km ray height (top of boundary layer), where strong multipath propagation exists and where the signal-to-noise ratio is very low. In summary, the CT differential transmission retrieval is found accurate throughout the free troposphere down to the top of the boundary layer in this low latitude case.

In order to illustrate the advantage of the computation of the CT differential transmission, we show an enlarged 1-km height segment of the measured amplitude of the wave field compared to the CT amplitude (Figure 20). The much better correlation of the CT amplitudes of the two channels, compared to the correlation of the measured amplitudes, is clearly visible. The decorrelation of CT amplitudes due to diffraction effects as mentioned above is noticed for scales below about 50 m. This has very small effect on the filtered differential transmission profiles, however, which are required for the atmospheric profiles retrieval at a resolution of near 1 km only.

Figures 21, 22, and 23 show the results of a simulation in presence of turbulence based on the ECMWF field in the high latitude region. According to Figure 15, the relative magnitude of turbulence $c(z)$ was here assumed 0.003 (0.3%) at a height of 2 km, log-linearly decreases to 0.0005 (0.05%) at a height of 6 km and kept constant above. Compared to the low latitude case, in this example the effects of multipath propagation are weak. The error of CT transmissions of a single channel is here less than 0.3 dB down to 4 km ray height ($\sim$3 km altitude) and the CT differential transmission error is less than 0.1 dB (2%) down to below 3.5 km ray height and less than 0.3 dB all the way down, respectively. Again the retrieval from amplitudes without CT pre-processing exhibits significantly inferior performance at all tropospheric heights (see top-left and bottom-left panels of Fig. 23).

Figure 24 shows the results of processing the same simulated event with, in addition, superimposing receiver noise with a magnitude of 67 dBHz above atmosphere. In this example, the influence of the measurement noise is significantly smaller than in the low latitude case above, since the lower

troposphere attenuation is much weaker retaining significantly more signal-to-noise ratio and since there is essentially no multipath propagation. The transmission retrieval performance is found not to be limited by the noise down towards the surface in this case.

Figures 25 (turbulence without receiver noise) and 26 (turbulence and receiver noise), finally, show the results for the high-latitude event under the same conditions as above for Figures 23 and 24, but the anisotropy coefficient of the turbulence reduced from $q = 20$ to $q = 10$. This does, according to this single trial (very computationally demanding), not significantly change the retrieval error overall, though some evidence is seen for improvement below 5 km in the lower troposphere.

Additional simulations, including closer towards isotropy of turbulence, will be useful in the future. As noted above, from existing theoretical and experimental evidence it is expected that the effects of turbulence in the occultation data will decrease with anisotropy coefficients getting smaller than $q = 10$, i.e., cases shown here should be upper bound estimates of what would be the effect of more isotropic turbulence. The improvement indicated in the lower troposphere in the $q = 10$ case compared to the $q = 20$ case is in line with this expectation but further simulations will be helpful to verify this evidence.

4 Discussion of Potential Unmodeled Errors

In the numerical simulations we assumed that the real part of the atmospheric refractivity is non-dispersive. Being rigorous, the real refractivity is not perfectly non-dispersive over several GHz spacing: 1) there is the small influence of the 22 GHz water vapor line also on real refractivity (even in clear air), 2) droplets (liquid clouds and rain) and ice crystals (ice clouds) affect real refractivity (scattering).

To quantify this effect, we computed a worst-case difference between the real refractivity at 10 and 22.6 GHz (the low and high channels of the ACE+ mission concept), assuming 30 mbar water vapor pressure, 5 g/m^3 liquid water content, and a heavy rain rate of 20 mm/h (ice water content can be ignored as generally too small for any appreciable contribution). This results in a real refractivity difference $\Delta N \approx 0.25$ N units. Because our method is based on the CT technique, where bending angles and absorption are computed as functions of impact parameter, we need to estimate the separation of two rays for the two frequency channels, with the same impact parameter. The ray separation at the perigee point can be estimated as $10^{-6} r_E \Delta N \approx 1.5$ m, where $r_E \approx 6370$ km is the Earth's radius. Obviously,

this effect is very small, in all practical cases clearly < 1 m, and will not result in any visible errors in the retrieved differential transmission (relative error of impact parameter < 1 m/6370000 m). Under conditions of heavy rain, transmission for 10–22.6 GHz frequencies cannot be accurately retrieved for a different reason, because strong absorption will severely degrade the signal-to-noise ratio of the measured signal. Rain effects will typically be of relevance below 2–3 km only, however.

In the numerical simulation we did not model atmospheric particulates, such as clouds, i.e., the non-clear-air atmosphere. While these can significantly affect absorption, this is not expected to be a problem, because absorption (whether gaseous or particulate) is not essential for the technique introduced, which corrects turbulence effects rooting in real refractivity rather than absorption (imaginary refractivity).

One more factor that could degrade the performance of the differential method is the ionosphere. Ionospheric errors can result from horizontal inhomogeneities in the ionosphere. For a spherically symmetric ionosphere two tropospheric rays with the same impact parameter will have the same perigee point. Horizontal inhomogeneity in the ionosphere will result in additional impact parameter perturbation, which will depend on the frequency. Worst-case perturbations of the impact parameter due to the ionosphere in L band (GPS radio occultations) have been estimated as $\sim$50 m (e.g., [*Gorbunov et al.*, 2002]). In the X/K band, the influence of the ionosphere is approximately 100 times smaller. Therefore, the ionospheric effect will also amount to < 1 m ray separation in virtually all cases, which is negligibly small.

5 Conclusions and Outlook

Processing X/K band radio occultation data in presence of turbulence poses a significant challenge, due to the scintillations imposed by the turbulence in the measured amplitude profiles. Retrieval of transmissions thus requires special provisions in the processing to correct for the scintillations. To this end, in earlier transmission retrieval approaches, a possibility was discussed of retrieving differential absorption from the direct ratio of measured amplitudes for two different (closely spaced) frequency channels, $|u_1(t)|$ and $|u_2(t)|$. Here we discussed an advanced differential method of retrieval of atmospheric transmissions based on the ratio of the CT amplitudes $\left|\hat{\Phi}u_1(p)\right|$ and $\left|\hat{\Phi}u_2(p)\right|$.

The new method results in much more accurate correction for turbulence scintillations, as compared to taking the direct ratio of the measured wave fields. This is due to the following reasons: 1) The CT mapping corrects for diffraction and multipath propagation effects, 2) The resulting transformed

field is independent from diffraction except for small scales below about 50 m. 3) The ratio of the transformed amplitudes then further corrects for small-scale scintillations and effects of the non-sphericity of the atmosphere. 4) The new method does not impose any significant restriction for the frequency difference Δf between the channels, and there is no requirement that Δf is small (e.g., clearly smaller than 1 GHz). This has important technical advantages and provides very good differential transmission sensitivity if spacings of a few GHz are chosen (e.g., 10 and 17 GHz or 17 and 20 GHz, or similar).

In order to assess the residual errors of the advanced method, we performed numerical simulations with different models of the atmospheric refractivity field in a rigorous forward-inverse modeling framework, including explicit high-resolution turbulence modeling. Different models such as smooth 3D ECMWF analysis fields and high-resolution radio sonde profiles were used as background, both without and with turbulence superposed. These numerical simulations, for which deliberately rather strong turbulence magnitudes were assumed together with magnitudes estimated from real high resolution radiosonde data, showed the high capabilities of the CT differential method.

We also performed numerical simulations which in addition included a model of receiver noise at a realistic level (carrier-to-noise 67 dBHz, ACE+ baseline). The influence of the noise is only significant below a ray impact height of 4 km (below 2–3 km altitude), where the carrier-to-noise ratio is becoming very low due to strong absorption and defocusing in the lower troposphere. The carrier-to-noise ratio of 67 dBHz was found just adequate. In this context also 1 kHz sampling rate was found the minimum required rate for adequate wave optics processing of X/K band occultation data. Effects of small amplitude drifts of 0.5% over 20 sec (ACE+ specification for maximum drift) were also assessed and found of minor relevance compared to thermal noise and of no further concern in the context of transmission retrievals.

The most realistic cases with ECMWF analysis fields as background, and with turbulence estimated from high-res radiosonde data and thermal receiver noise superposed, showed that the CT processing as part of the bending angle and transmission retrieval leads to transmission accuracies vastly superior to direct exploitation of amplitudes or amplitude ratios. This holds for both single channel transmissions and differential transmissions. The 10–17 GHz differential transmissions from CT processing were found, under the conditions assumed, to be accurate to better than 5% even in the lower troposphere at low latitudes down to the boundary layer. In comparison, without CT processing the errors were found to exceed 10% below 6 to 8 km already. At high latitudes, CT differential transmissions are accurate down towards the surface.

Processing differential transmissions further to imaginary refractivity and, in turn, together with real refractivity derived from bending angles, to atmospheric profiles is a procedure identical to using single-channel transmissions [*Kursinski et al.*, 2002; *Kirchengast et al.*, 2004b, a]. Due to the differencing, there is one differential transmission profile less, however, than single-channel transmission profiles. In the case of ACE+ with 3 frequencies this implies availability of two differential transmission profiles (9.7–17.25 GHz, 17.25–22.6 GHz), which are still sufficient in combination with real refractivity to separate water vapor and liquid water from temperature down into the lower troposphere, as long as the 17.25–22.6 GHz differential transmission has sufficient signal-to-noise ratio. Since in tropical, cloudy situations it will probably find a lower limit at about 5 km height, it is advisable that a robust differential transmission system actively targeting the lower troposphere with the aim to minimize use of best-fit temperature extrapolation includes an additional frequency at 13.5 GHz. In this case the 22.6 GHz measurement can be terminated near 5 km and the 9.7–13.5 GHz and 13.5–17.25 GHz differential transmissions will furnish humidity and liquid water separation capability below 5 km.

An analogous argument could be made also for a 20.2 GHz channel in between 17.25 GHz and 22.6 GHz, to ensure two simultaneous differential transmissions above about 8 km. Here the argument has low substance, however, since liquid water amounts are generally so small above 8 km that separation is not required. Moreover, while not specifically discussed in this study focusing on the lower and middle troposphere, it appears that above about 10 km, where the 17.25–22.6 GHz differential transmission might increasingly loose sensitivity, CT-derived single-channel transmission accuracy is adequate so that the 22.6 GHz channel can be directly used at these heights also in presence of turbulence. Note that for all cases with small turbulence, which have not been in the focus of this study but which are expected to comprise about half of the ACE+ profiles, the CT-derived single-channel transmissions are expected to be of adequate accuracy for all channels.

In the future, in work beyond confirming and consolidating the ACE+ feasibility as done here, the present study can be refined and expanded along several lines. Based on further refined assessments of realistic refractivity turbulence strengths, derived from assessing the rms of small-scale fluctuations in high-resolution radiosonde profiles at different geographic locations, a quantitative assessment would be possible which fraction of profiles might need differential transmission instead of single-channel transmission processing. In this context also the potential benefit from a 13.5 GHz channel could be explored as well as the presumably appealing cost-benefit ratio of a lower-cost 17.25–20.2–22.6 GHz single-antenna K band system, which would be de-

signed to focus on the atmosphere above 5 km, for independent temperature-humidity-pressure measurements, where the most important climate science needs for the data exist.

In connection with this, the refractivity and atmospheric profiles retrieval performance based on differential rather than single-channel transmission can be quantitatively assessed, for different levels of turbulence strength. Also, further efforts to perform the explicit turbulence modeling at even higher resolution (e.g., down to an inner scale of turbulence of 10 m instead of 30 m, and down to an-isotropy coefficients as small as 5) will be useful, for further checking the existing theoretical and experimental results, and indications from the present baseline results, that residual errors will become smaller when approaching isotropic turbulence and that turbulence scales < 30 m will have insignificant effect on residual transmission errors.

Independent of such useful further work, there is clear evidence from the present study already that in those turbulent cases where single-channel transmissions might be too noisy to be processed directly, the use of CT differential transmissions is an adequate alternative. It can be expected, based on the experience from single-channel transmission processing [*Kirchengast et al.*, 2004b], that also use of differential transmissions will allow to meet X/K band occultation observation requirements such as laid out for ACE+. Moreover, given the evidence from this study, the new approach will allow pushing the typical height limits of needing auxiliary temperature information in the lower troposphere significantly farther down towards the boundary layer than baselined in the *ESA* [2004] assessment. A simpler 17.25–20.2–22.6 GHz K band system targeting > 5 km (and penetrating the lower troposphere on a best-effort basis, depending on absorption strength) is expected to need no auxiliary temperature information at all.

Acknowledgments. The authors gratefully acknowledge valuable discussions related to this work with A.S. Gurvich (IAP Moscow, Russia), S.V. Sokolovskiy (UCAR, Boulder, CO, USA), F. Cuccoli (Univ. of Florence, Italy), S. Buehler (Univ. of Bremen, Germany), P. Silvestrin (ESA/ESTEC, Noordwijk, Netherlands), and further colleagues of the ESA-ACEPASS study team. S. Buehler is in particular also thanked for his kind contribution of the basic St.Helena and Lerwick turbulence rms figures (Figures 14 and 15). The work was funded by ESA under ESA/ESTEC Contract No. 16743/02/NL/FF.

References

Buehler, S., IEP technical note on calculating the structure constant – calculating Cn2 from high resolution radiosonde profiles, *Acepass tech. note to esa./estec – jul. 2004*, IEP, Univ. of Bremen, Germany, 2004.

ESA, ACE+ – atmosphere and climate explorer (4th report of reports for mission selection, the six candidate earth explorer missions), *ESA Spec. Publ. SP 1279(4)*, ESA Publ. Division, ESTEC, Noordwijk, Netherlands, 2004.

Facheris, L., and F. Cuccoli, Analysis of differential spectral attenuation measurements applied to a LEO-LEO link, *ESA-ACEPASS Report (contract 16743/02/NL/FF)*, Inst. of Elect. and Telecommunications, Univ. of Florence, 2003.

Fritts, D. C., and M. J. Alexander, Gravity waves dynamics and effects in the middle atmosphere, *Reviews of Geophysics*, *41*, 1/1003, doi:10.1029/2001RG000,106, 2003.

Fritts, D. C., and T. E. VanZandt, Spectral estimates of gravity wave energy and momentum fluxes. part 1: Energy dissipation, acceleration, and constrains, *Journal of the Atmospheric Sciences*, *50*, 3685–3694, 1993.

Fritts, D. C., T. Tsuda, T. Sato, S. Fukao, and S. Kato, Observational evidence of a saturated gravity wave spectrum in the troposphere and lower stratosphere, *J. Atmos. Sci.*, *45*, 1741 1758, 1988.

Gorbunov, M. E., Canonical transform method for processing GPS radio occultation data in lower troposphere, *Radio Sci.*, *37*, 9–1–9–10, doi:10.1029/2000RS002,592, 2002a.

Gorbunov, M. E., Radio-holographic analysis of Microlab-1 radio occultation data in the lower troposphere, *J. Geophys. Res. - Atm.*, *107*, 7–1–7–10, doi: 10.1029/2001JD000,889, 2002b.

Gorbunov, M. E., and A. S. Gurvich, Microlab-1 experiment: Multipath effects in the lower troposphere, *Journal of Geophysical Research*, *103*, 13,819–13,826, 1998.

Gorbunov, M. E., and L. Kornblueh, Analysis and validation of GPS/MET radio occultation data, *Journal of Geophysical Research*, *106*, 17,161–17,169, 2001.

Gorbunov, M. E., and K. B. Lauritsen, Canonical transform methods for radio occultation data, *Scientific Report 02-10*, Danish Meteorological Institute, Copenhagen, Denmark, 2002, http://www.dmi.dk/dmi/Sr02-10.pdf.

Gorbunov, M. E., and K. B. Lauritsen, Analysis of wave fields by Fourier Integral Operators and its application for radio occultations, *Radio Sci.*, *39*, RS4010, doi:10.1029/2003RS002,971, 2004, accepted.

Gorbunov, M. E., A. S. Gurvich, and A. V. Shmakov, Back-propagation and radio-holographic methods for investigation of sporadic ionospheric E-layers from Microlab-1 data, *Int. J. Remote Sens.*, *23*, 675 – 685, 2002.

Gorbunov, M. E., H.-H. Benzon, A. S. Jensen, M. S. Lohmann, and A. S. Nielsen, Comparative analysis of radio occultation processing approaches based on Fourier integral operators, *Radio Sci.*, *39*, RS6004, doi:10.1029/2003RS002,916, 2004.

Gurvich, A. S., Fluctuations during observations of extraterrestrial sources from space through the atmosphere of the earth, *Radiophysics and Quantum Electronics*, *27*, 665, 1984.

Gurvich, A. S., Scintillation spectra during observations of star obscurations by the earth's atmosphere, *Atmospheric Optics*, *2*, 188, 1989.

Gurvich, A. S., and V. L. Brekhovskikh, Study of the turbulence and inner waves in the stratosphere based on the observations of stellar scintillations from space: A model of scintillation spectra, *Waves in Random Media*, *11*, 163–181, 2001.

Gurvich, A. S., and I. P. Chunchuzov, Parameters of the fine density structure in the stratosphere obtained from spacecraft observations of stellar scintillations, *J. Geophys. Res.*, *108*, 4166, doi:10.1029/2002JD002,281, 2003.

Gurvich, A. S., and I. P. Chunchuzov, Estimates of characteristic scales in the spectrum of internal waves in the stratosphere obtained from space observations of stellar scintillations, *J. Geophys. Res.*, *110*, 3114, doi:10.1029/2004JD005,199, 2005.

Jensen, A. S., M. S. Lohmann, H.-H. Benzon, and A. S. Nielsen, Full spectrum inversion of radio occultation signals, *Radio Sci.*, *38*, 6–1–6–15, doi: 10.1029/2002RS002,763, 2003.

Jensen, A. S., M. S. Lohmann, A. S. Nielsen, and H.-H. Benzon, Geometrical optics phase matching of radio occultation signals, *Radio Sci.*, *39*, RS3009, doi: 10.1029/2003RS002,899, 2004.

Kan, V., S. S. Matyugov, and O. I. Yakovlev, The structure of stratospheric irregularities according to radio-occultation data obtained using satellite-to-satellite paths, *Izvestiya VUZov, Radiofizika*, *XLV*, 652–663, 2002.

Kirchengast, G., J. Fritzer, M. Schwaerz, S. Schweitzer, and L. Kornblueh, The atmosphere and climate explorer mission ACE+: Scientific algorithms and performance overview, *Tech. Report for ESA/ESTEC No. 2/2004*, Inst. for Geophys., Astrophys., and Meteorol., Univ. of Graz, Austria, 2004a.

Kirchengast, G., S. Schweitzer, J. Ramsauer, J. Fritzer, and M. Schwaerz, Atmospheric profiles retrieved from ACE+ LEO-LEO occultation data: Statistical performance analysis using geometric optics processing, *Tech. Report for ESA/ESTEC No. 1/2004*, Inst. for Geophys., Astrophys., and Meteorol., Univ. of Graz, Austria, 2004b.

Kuhn, T., Atmospheric scintillation, *Acepass tech. note to esa/estec – feb. 2003*, IEP, Univ. of Bremen, Germany, 2003.

Kursinski, E. R., G. A. Hajj, S. S. Leroy, and B. Herman, The GPS radio occultation technique, *Terrestr. Atmosph. Ocean. Sci.*, *11*, 53–114, 2000.

Kursinski, E. R., S. Syndergaard, D. Flittner, D. Feng, G. Hajj, B. Herman, D. Ward, and T. Yunck., A microwave occultation observing system optimized to characterize atmospheric water, temperature and geopotential via absorption, *Journal of Atmospheric and Oceanic Technology*, *19*, 1897–1914, 2002.

Martin, J., Simulation of wave propagation in random media: theory and applications, in *Wave propagation in random media (scintillations)*, edited by V. I. Tatarskii, A. Ishimaru, and V. U. Zavorotny, pp. 463–486, SPIE - The International Society for Optical Engineering and Institute of Physics Publishing, Bellingham, Washington USA, Bristol and Philadelphia, 1992.

Rytov, S. M., Yu.A. Kravtsov, and V.I. Tatarskii, *Principles of Statistical Radiophysics, Vol. 4, Wave Propagation Through Random Media*, Springer, Berlin–Heidelberg, 1989.

Sokolovskiy, S. V., Tracking tropospheric radio occultation signals from low earth orbit, *Radio Sci.*, *36*, 483–498, 2001.

Vorob'ev, V. V., and T. G. Krasil'nikova, Estimation of the accuracy of the atmospheric refractive index recovery from Doppler shift measurements at frequencies used in the NAVSTAR system, *Izvestiya Academy of Sciences SSSR, Atmospheric and Oceanic Physics, English Translation*, *29*, 602–609, 1994.

Yakovlev, O. I., S. S. Matyugov, and I. A. Vilkov, Attenuation and scintillation of radio waves in the Earth's atmosphere from radio occultation experiment on satellite-to-satellite links, *Radio Science*, *30*, 591–602, 1995.

Yakovlev, O. I., S. S. Matyugov, and V. A. Anufriev, Scintillations of centimeter waves and the atmospheric irregularities from radio occultation data, *Radio Sci.*, *38*, doi: 10.1029/2000RS002,546, 2003.

Figures

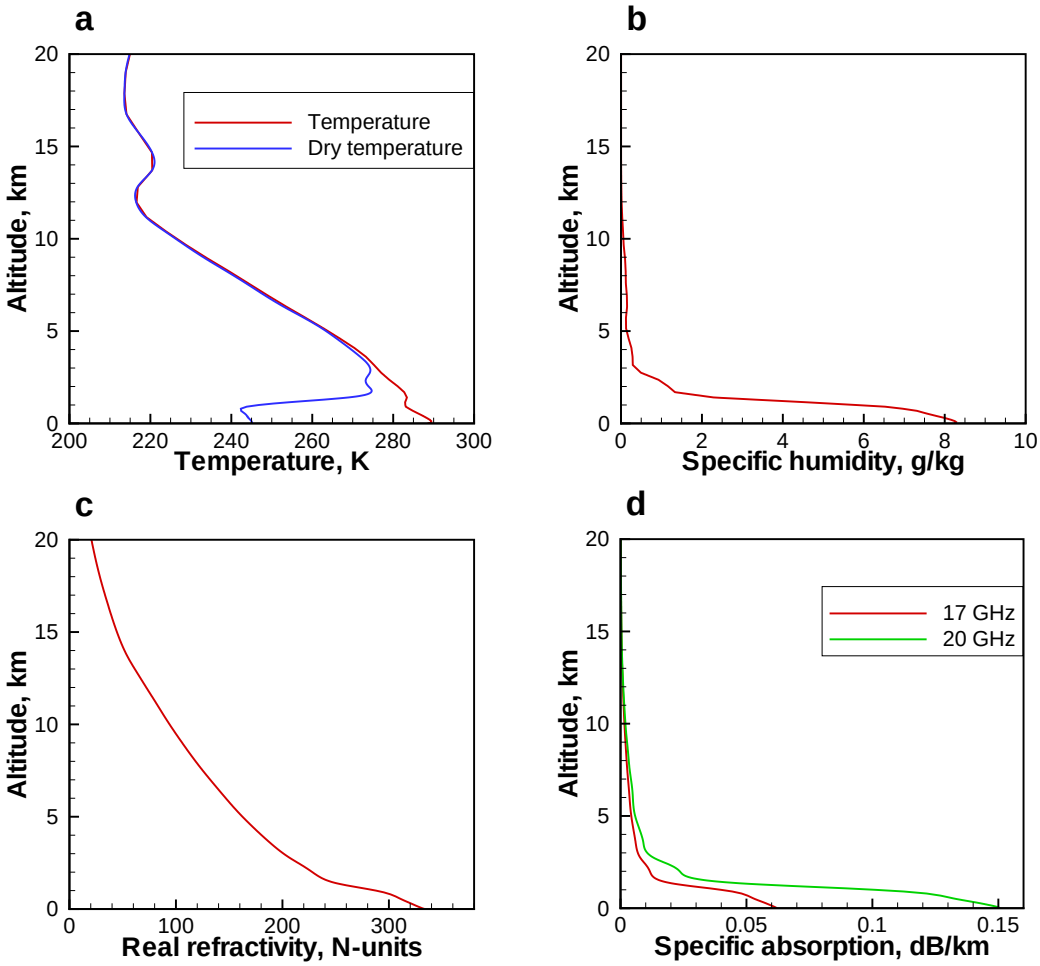

Figure 1: Simulated occultation event 0198, May 28, 2001, UTC 21:25, 52.8°N 2.2°E, frequency channels 17 and 20 GHz: (a) temperature, T, and dry temperature, T_{dry}, (b) specific humidity, q, (c) real refractivity, N, and specific absorptions, $(20/\ln 10)kN_I$, for the two frequencies.

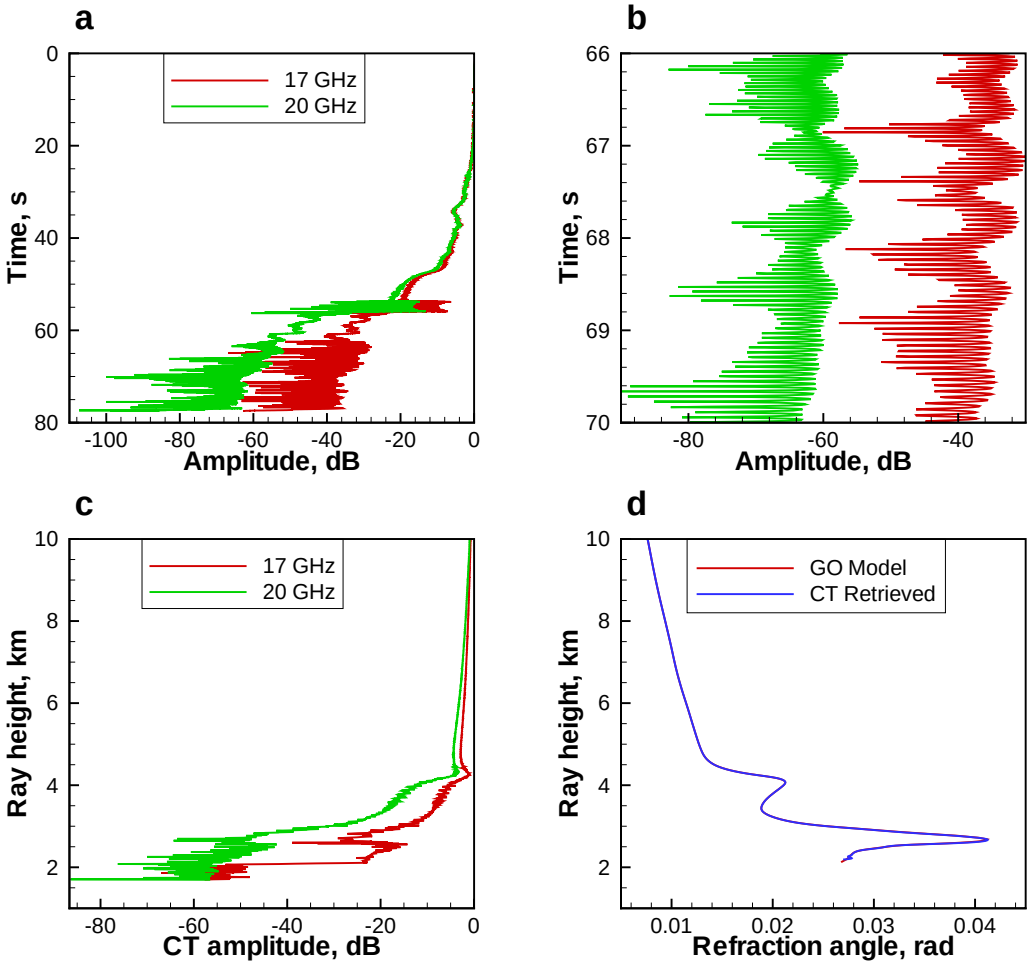

Figure 2: Simulated occultation event 0198, May 28, 2001, UTC 21:25, 52.8°N 2.2°E, frequency channels 17 and 20 GHz: (a) amplitudes in the two channels, (b) enlarged fragment of amplitude records in multipath area, (c) CT amplitudes for the two channels, and (d) refraction angles, computed by the GO model and retrieved by the CT method.

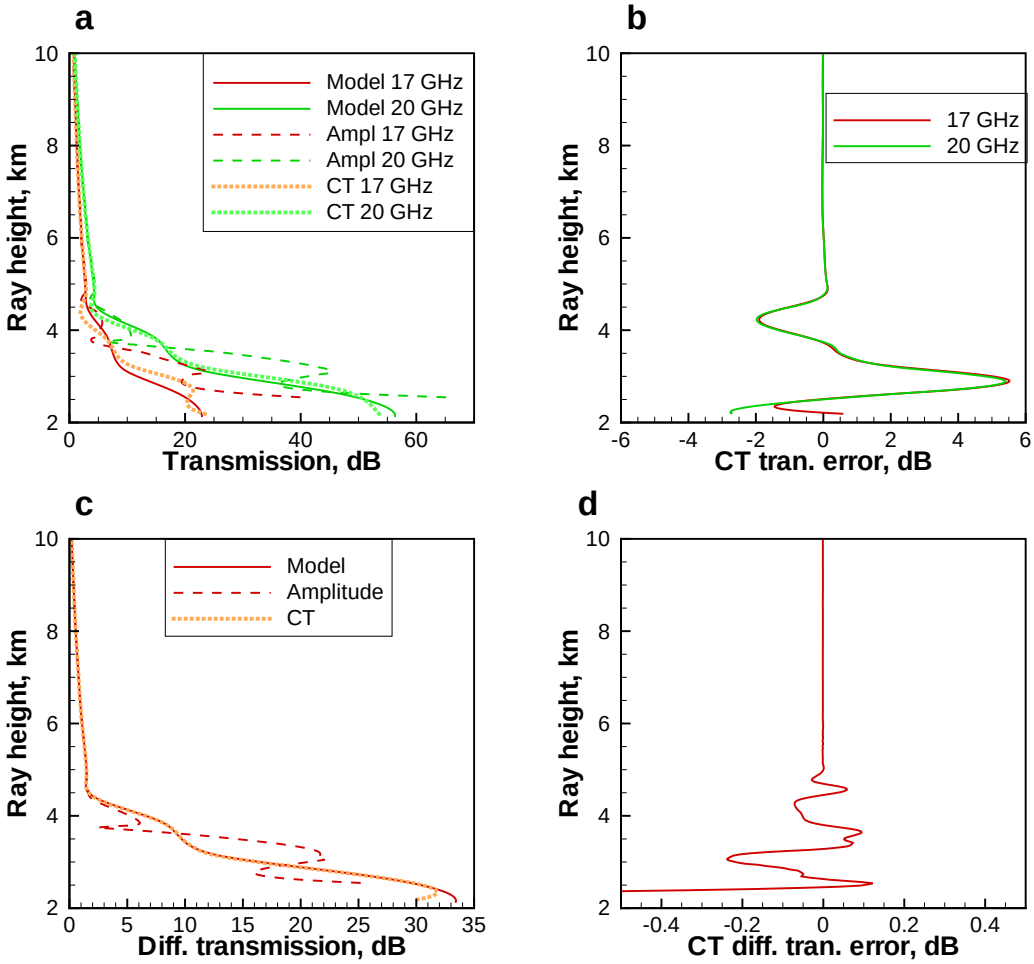

Figure 3: Simulated occultation event 0198, May 28, 2001, UTC 21:25, 52.8°N 2.2°E, frequency channels 17 and 20 GHz: (a) transmissions for the two channels, true model, computed from the amplitudes, and computed from the CT amplitudes, (b) errors of the CT transmission, (c) differential transmission, true model, computed from the amplitudes, and computed from the CT amplitudes, and (d) errors of the CT differential transmission.

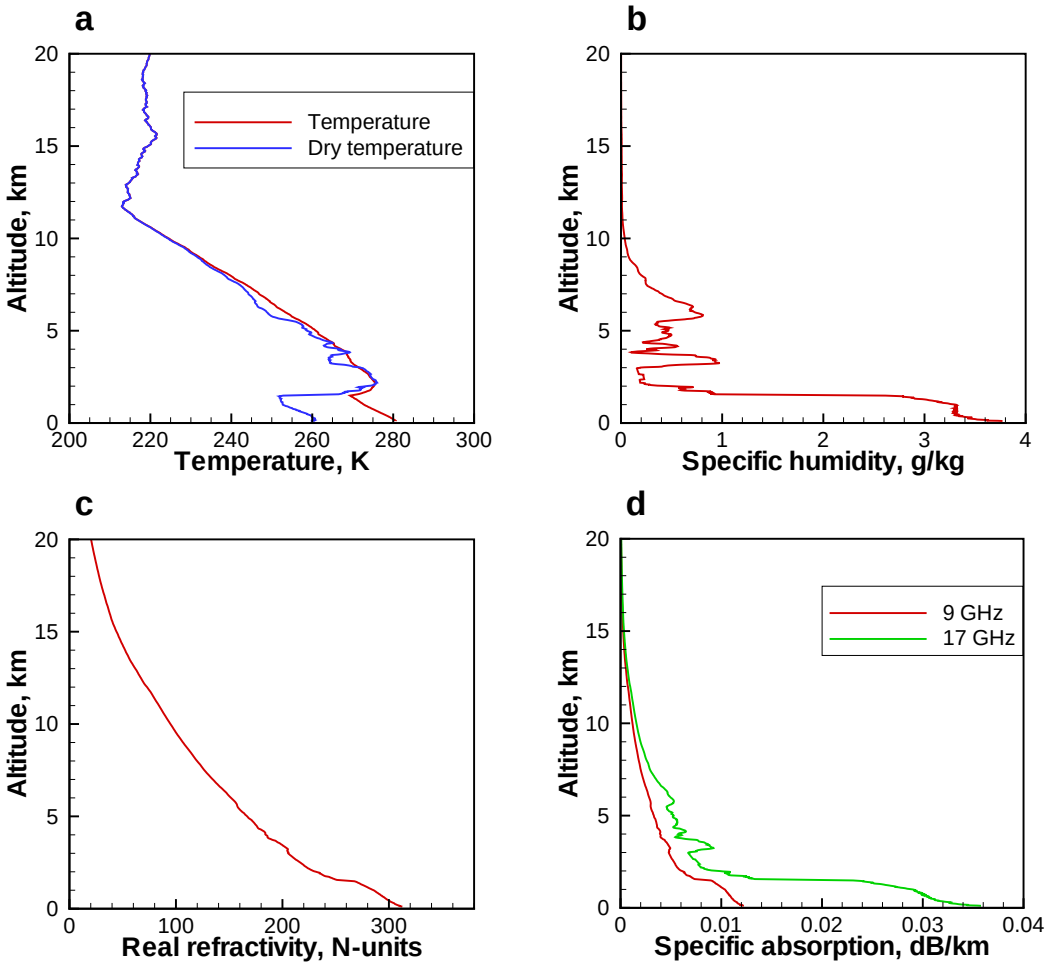

Figure 4: Simulated occultation event for a high-resolution radio sonde profiles, frequency channels 9 and 17 GHz: (a) temperature T and dry temperature T_{dry}, (b) specific humidity, q, (c) real refractivity, N, and specific absorptions, $(20/\ln 10)kN_I$, for the two frequencies.

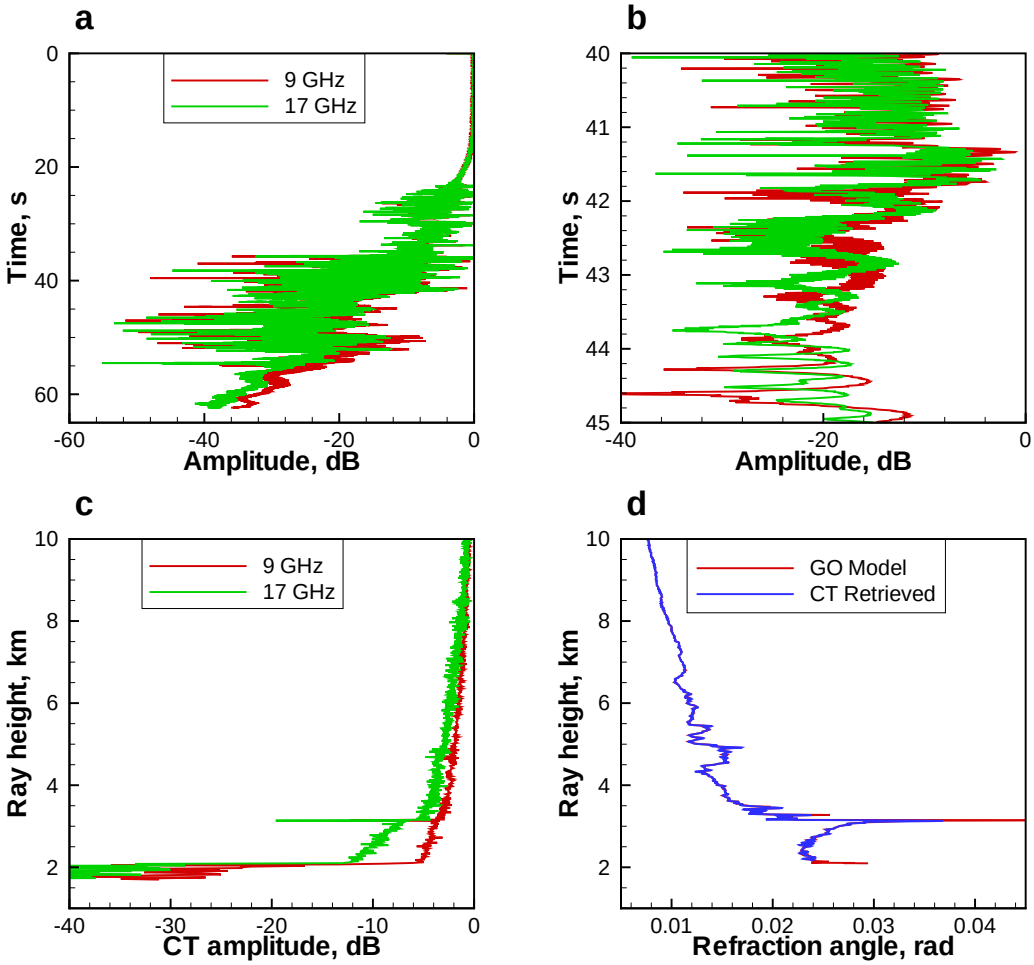

Figure 5: Simulated occultation event for a high-resolution radio sonde profiles, frequency channels 9 and 17 GHz: (a) amplitudes in the two channels, (b) enlarged fragment of amplitude records in multipath area, (c) CT amplitudes for the two channels, and (d) refraction angles, computed by the GO model and retrieved by the CT method.

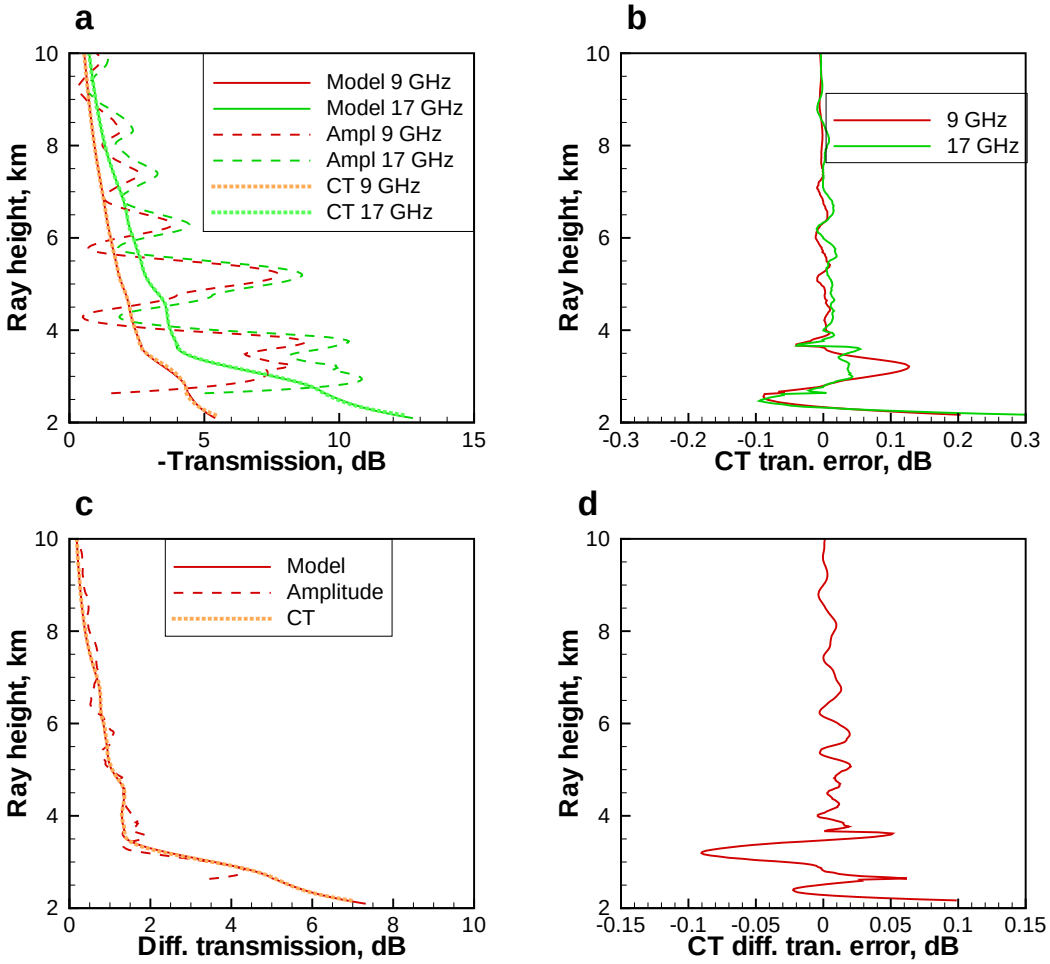

Figure 6: Simulated occultation event for a high-resolution radio sonde profiles, frequency channels 9 and 17 GHz: (a) transmissions for the two channels, true model, computed from the amplitudes, and computed from the CT amplitudes, (b) errors of the CT transmission, (c) differential transmission, true model, computed from the amplitudes, and computed from the CT amplitudes, and (d) errors of the CT differential transmission.

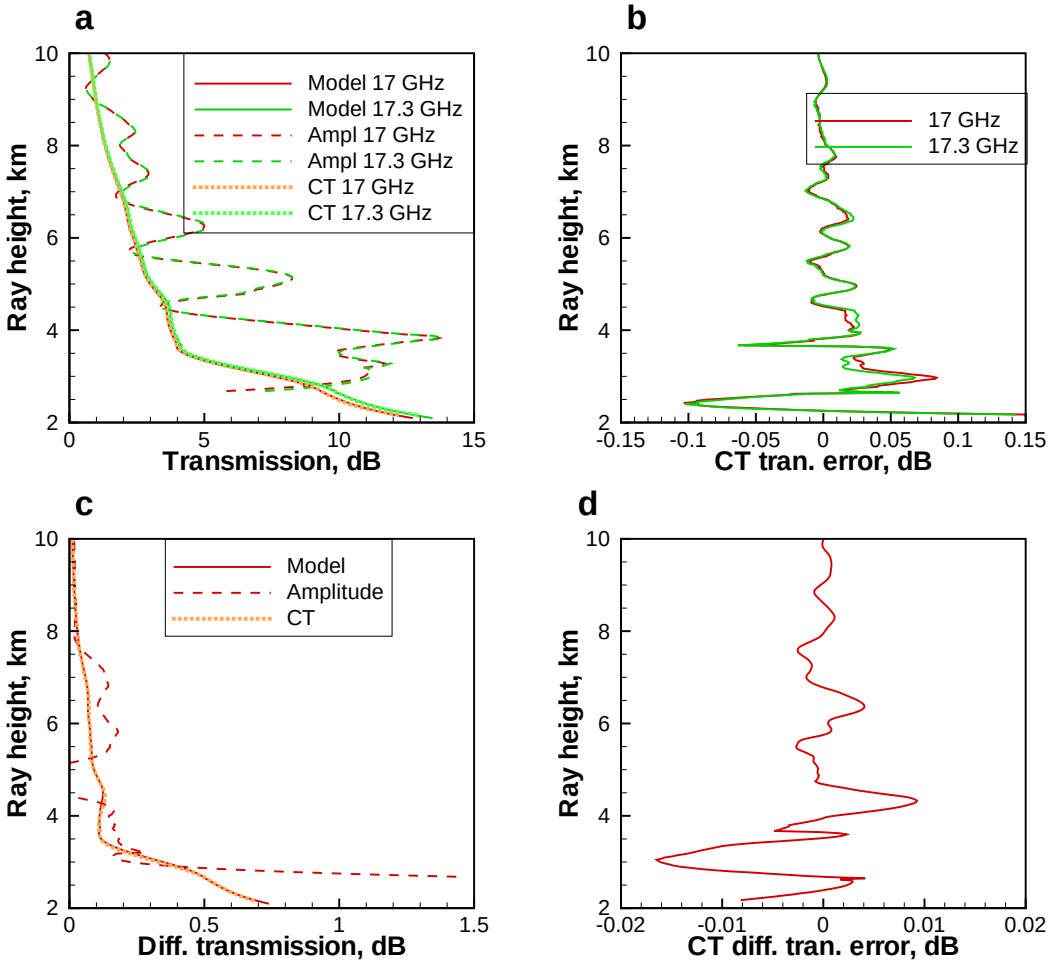

Figure 7: Simulated occultation event for a high-resolution radio sonde profiles, frequency channels 17 and 17.3 GHz: (a) transmissions for the two channels, true model, computed from the amplitudes, and computed from the CT amplitudes, (b) errors of the CT transmission, (c) differential transmission, true model, computed from the amplitudes, and computed from the CT amplitudes, and (d) errors of the CT differential transmission.

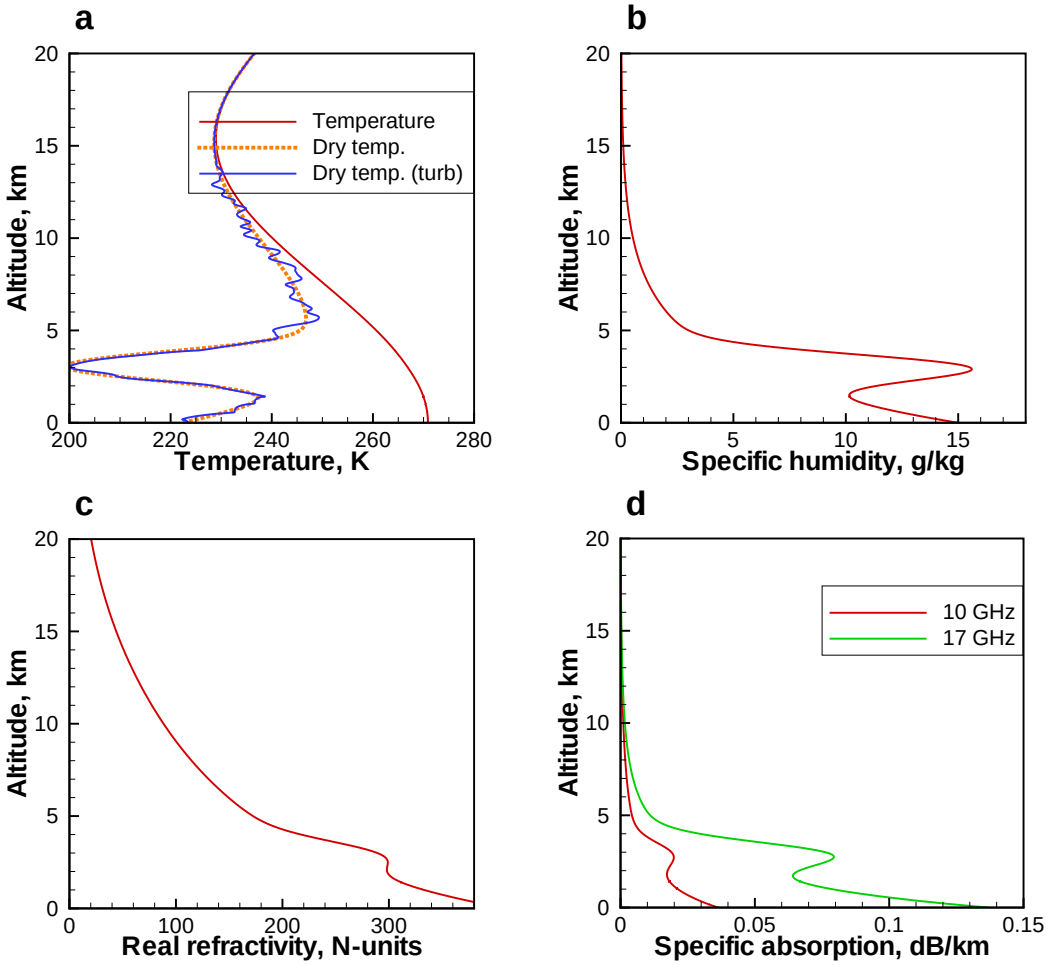

Figure 8: Simulated occultation event for a spherically symmetric model with superimposed Gaussian turbulence, frequency channels 10 and 17 GHz: (a) temperature T and dry temperature $T_{\rm dry}$ for the regular medium and dry temperature $T_{\rm dry}^{\rm (turb)}$ for the turbulent medium, (b) specific humidity, q, (c) real refractivity, N, and specific absorptions, $(20/\ln 10)kN_I$, for the two frequencies.

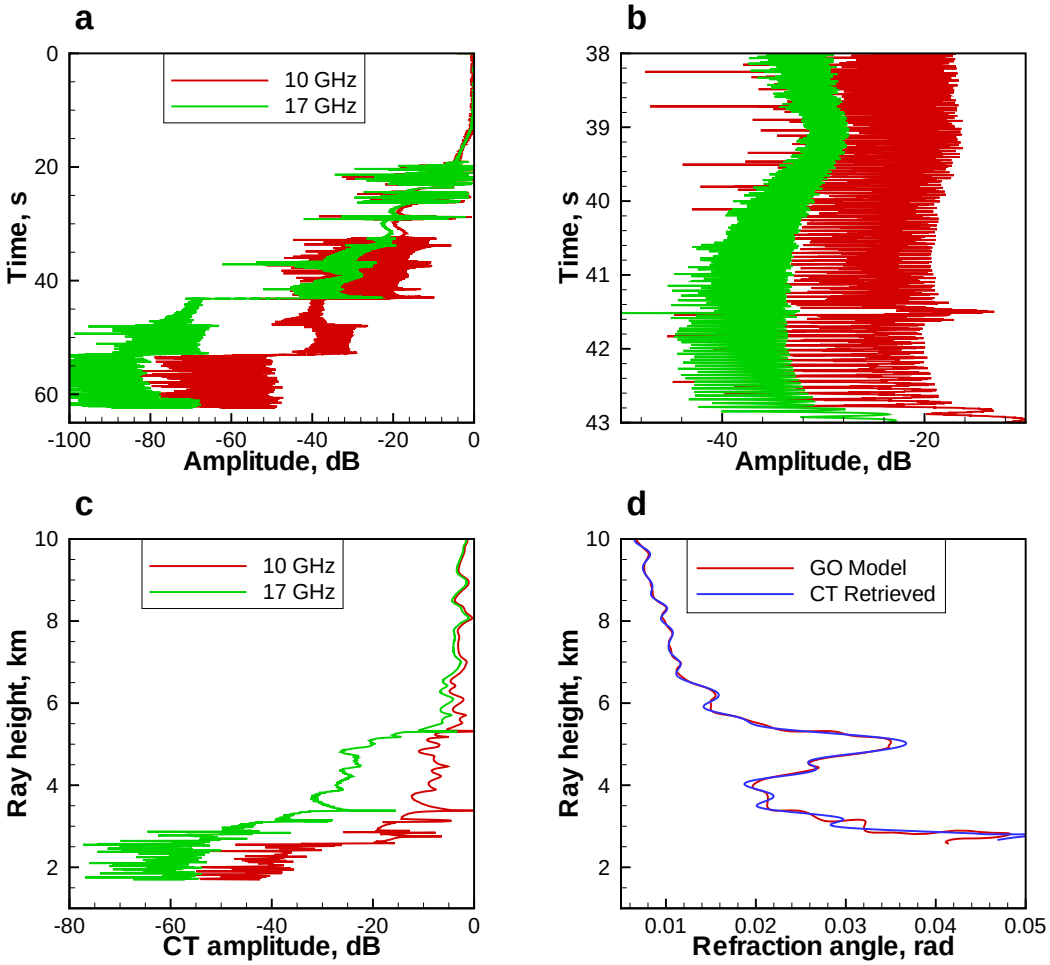

Figure 9: Simulated occultation event for a spherically symmetric model with superimposed Gaussian turbulence, frequency channels 10 and 17 GHz: (a) amplitudes in the two channels, (b) enlarged fragment of amplitude records in multipath area, (c) CT amplitudes for the two channels, and (d) refraction angles, computed by the GO model and retrieved by the CT method.

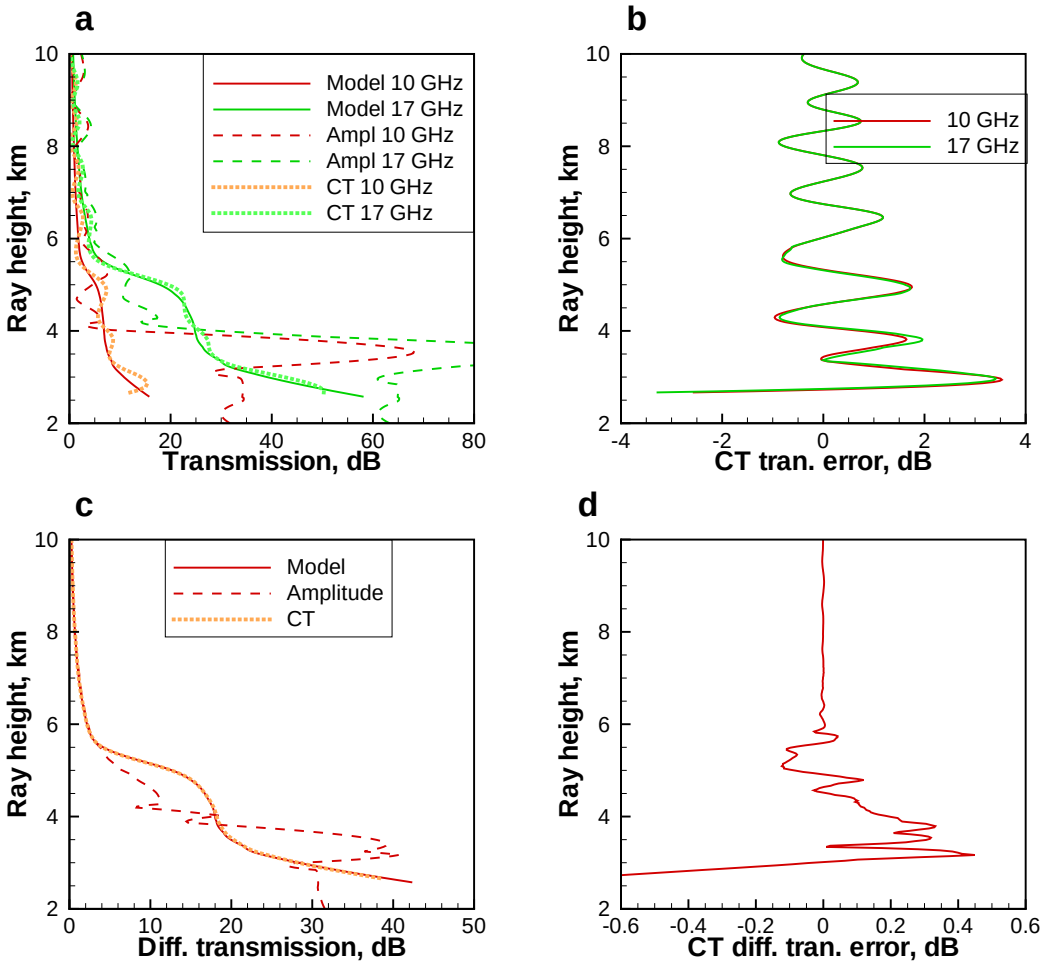

Figure 10: Simulated occultation event for a spherically symmetric model with superimposed Gaussian turbulence, frequency channels 10 and 17 GHz: (a) transmissions for the two channels, true model, computed from the amplitudes, and computed from the CT amplitudes, (b) errors of the CT transmission, (c) differential transmission, true model, computed from the amplitudes, and computed from the CT amplitudes, and (d) errors of the CT differential transmission.

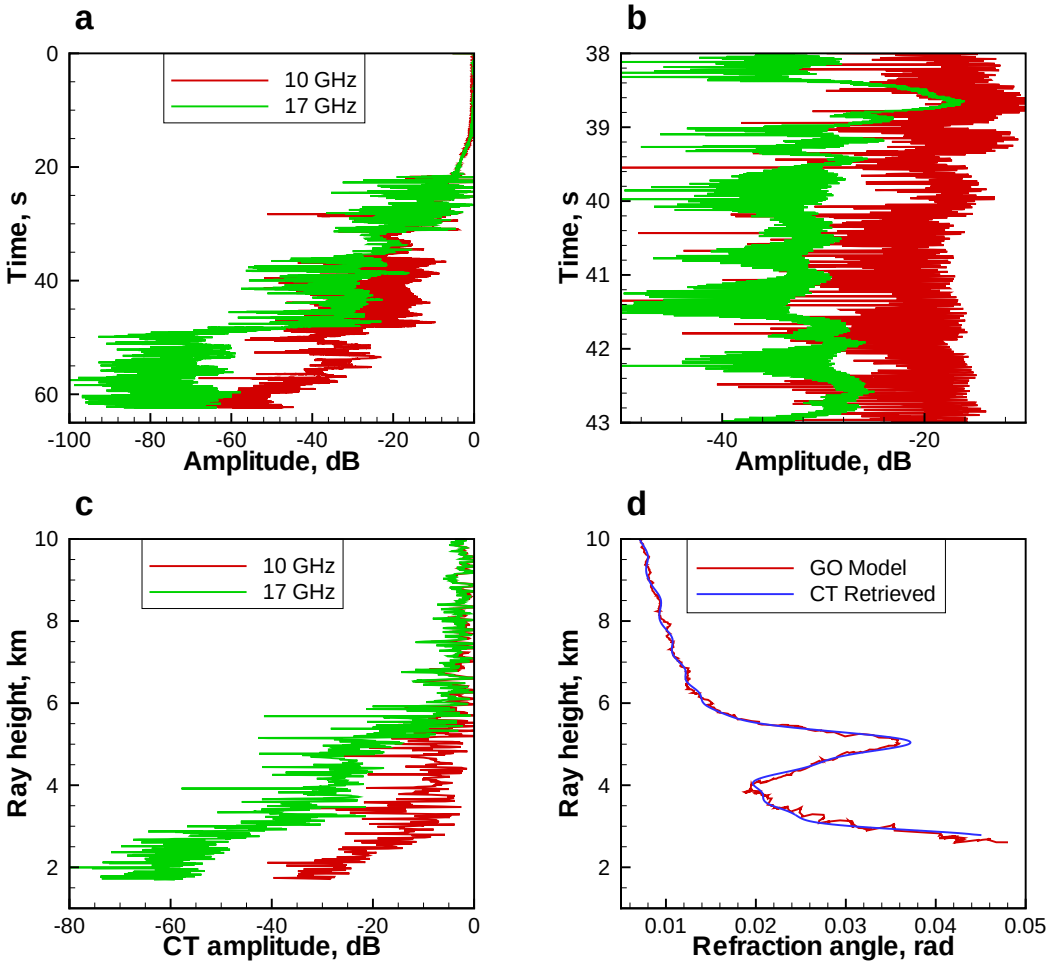

Figure 11: Simulated occultation event for a spherically symmetric model with superimposed power turbulence, frequency channels 10 and 17 GHz: (a) amplitudes in the two channels, (b) enlarged fragment of amplitude records in multipath area, (c) CT amplitudes for the two channels, and (d) refraction angles, computed by the GO model and retrieved by the CT method.

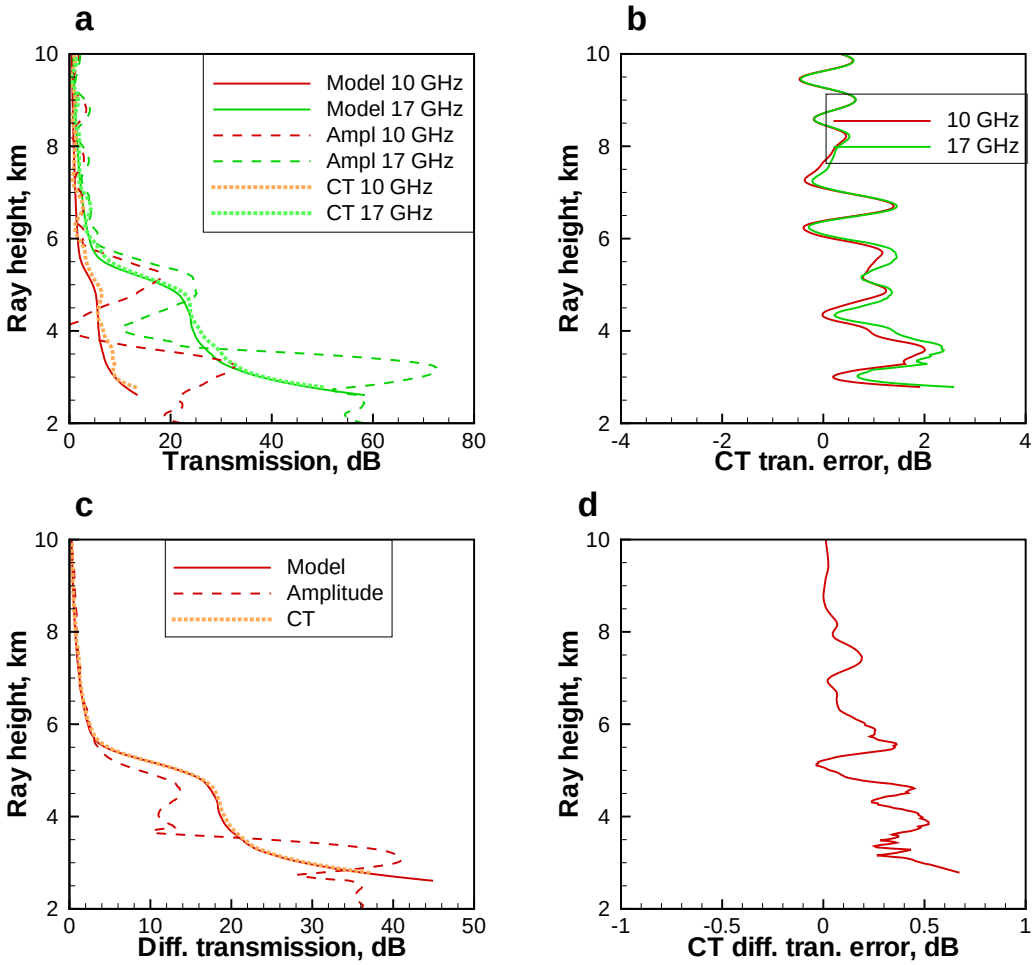

Figure 12: Simulated occultation event for a spherically symmetric model with superimposed power turbulence, frequency channels 10 and 17 GHz: (a) transmissions for the two channels, true model, computed from the amplitudes, and computed from the CT amplitudes, (b) errors of the CT transmission, (c) differential transmission, true model, computed from the amplitudes, and computed from the CT amplitudes, and (d) errors of the CT differential transmission.

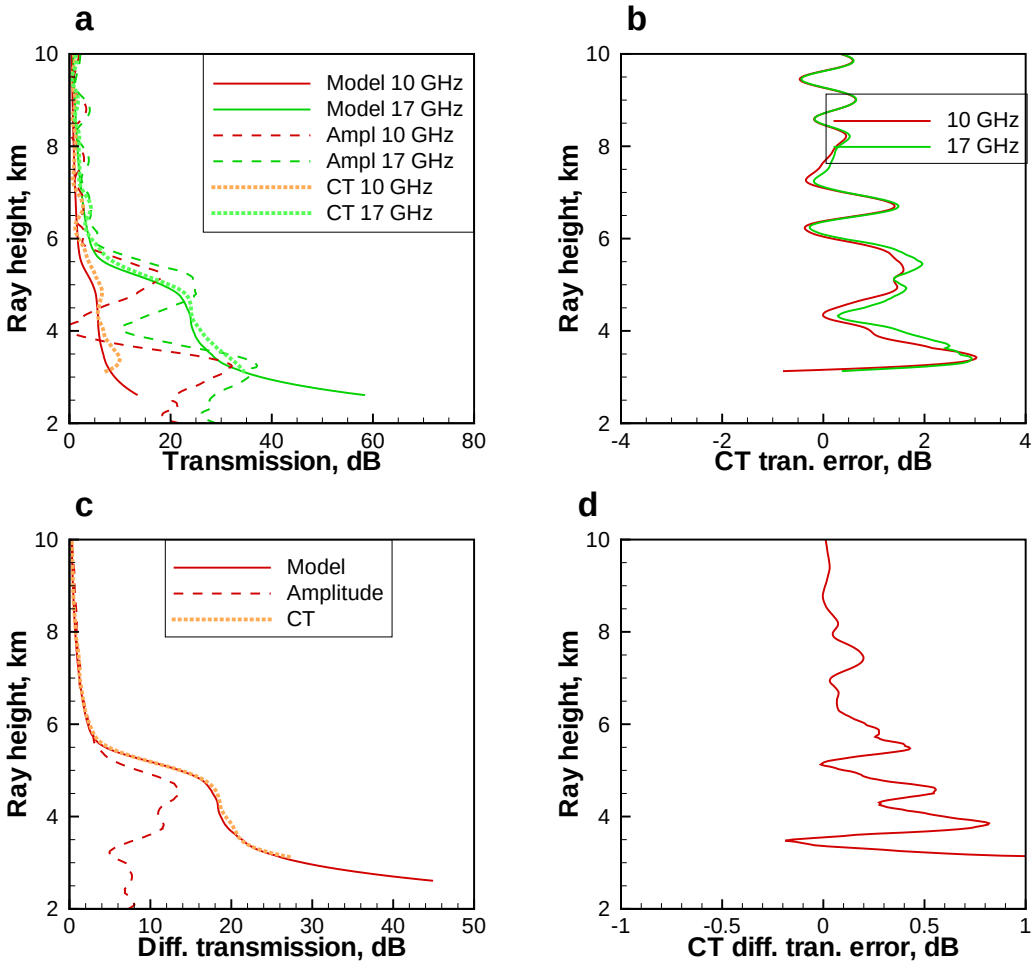

Figure 13: Simulated occultation event for a spherically symmetric model with superimposed power turbulence and random noise, frequency channels 10 and 17 GHz: (a) transmissions for the two channels, true model, computed from the amplitudes, and computed from the CT amplitudes, (b) errors of the CT transmission, (c) differential transmission, true model, computed from the amplitudes, and computed from the CT amplitudes, and (d) errors of the CT differential transmission.

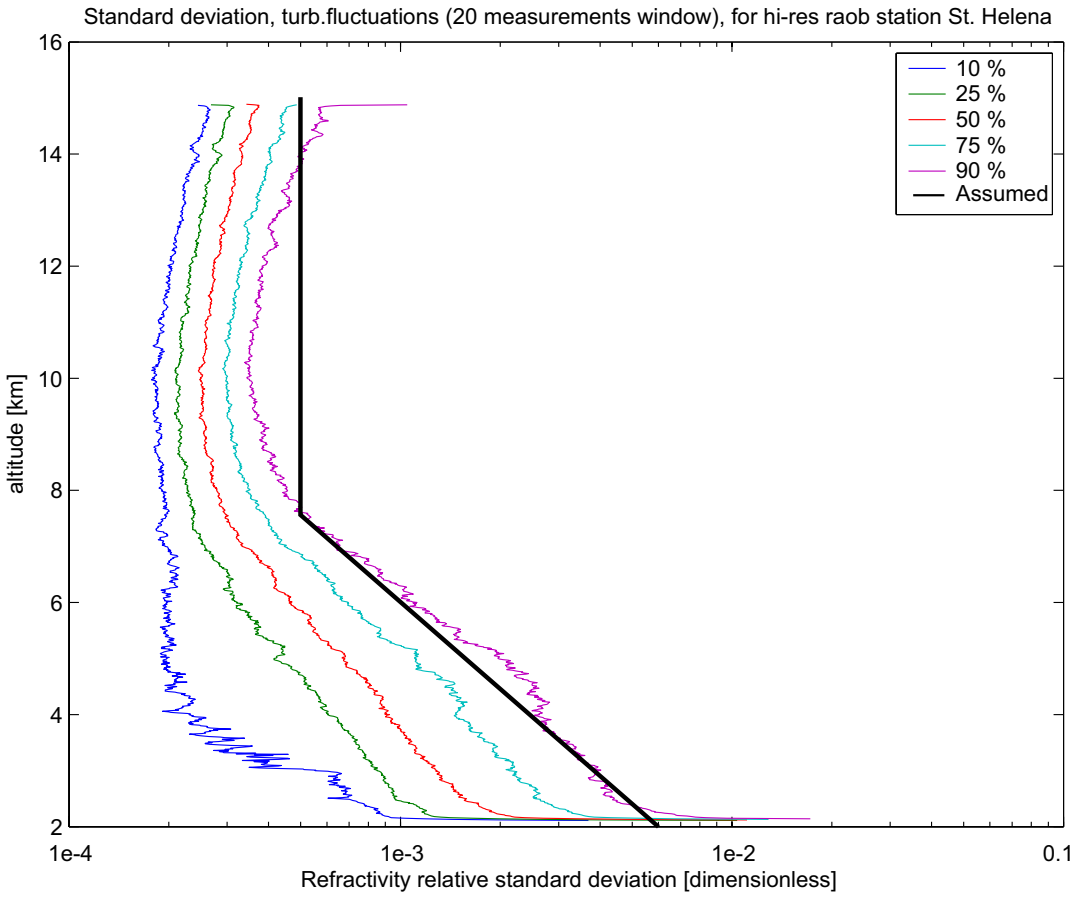

Figure 14: Estimation of rms profiles of turbulent fluctuations on the basis of a dataset of hi-res raob profiles observed at St.Helena ("low latitude"; 15.6°S, 5.4°W): Median profile (50%) und different percentiles. The profile "Assumed" (heavy black line), meant to roughly reflect the upper decile (90%), is the one used for the turbulence modeling in this study. (Figure courtesy of S. Buehler, Univ. of Bremen, Germany; adapted)

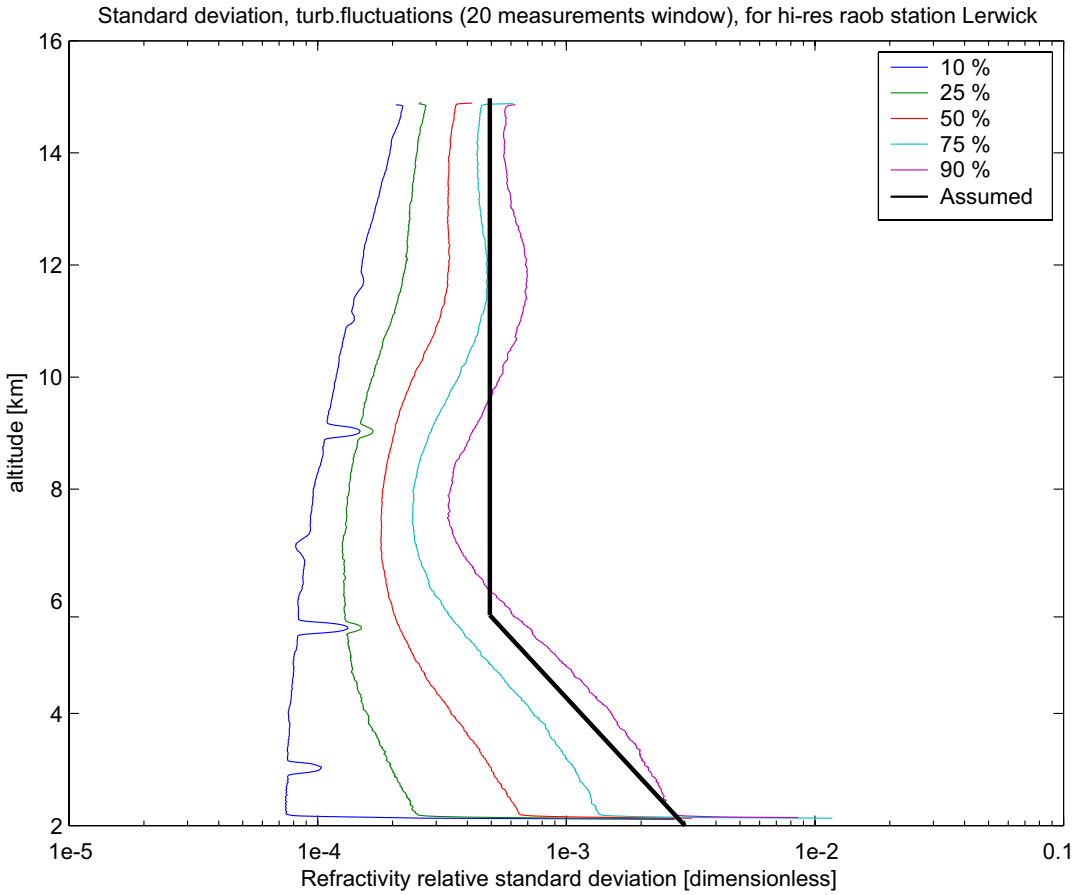

Figure 15: Estimation of rms profiles of turbulent fluctuations on the basis of a dataset of hi-res raob profiles observed at Lerwick ("high latitude"; 60.1°N, 1.2°W): Median profile (50%) und different percentiles. The profile "Assumed" (heavy black line), meant to roughly reflect the upper decile (90%), is the one used for the turbulence modeling in this study. (Figure courtesy of S. Buehler, Univ. of Bremen, Germany; adapted)

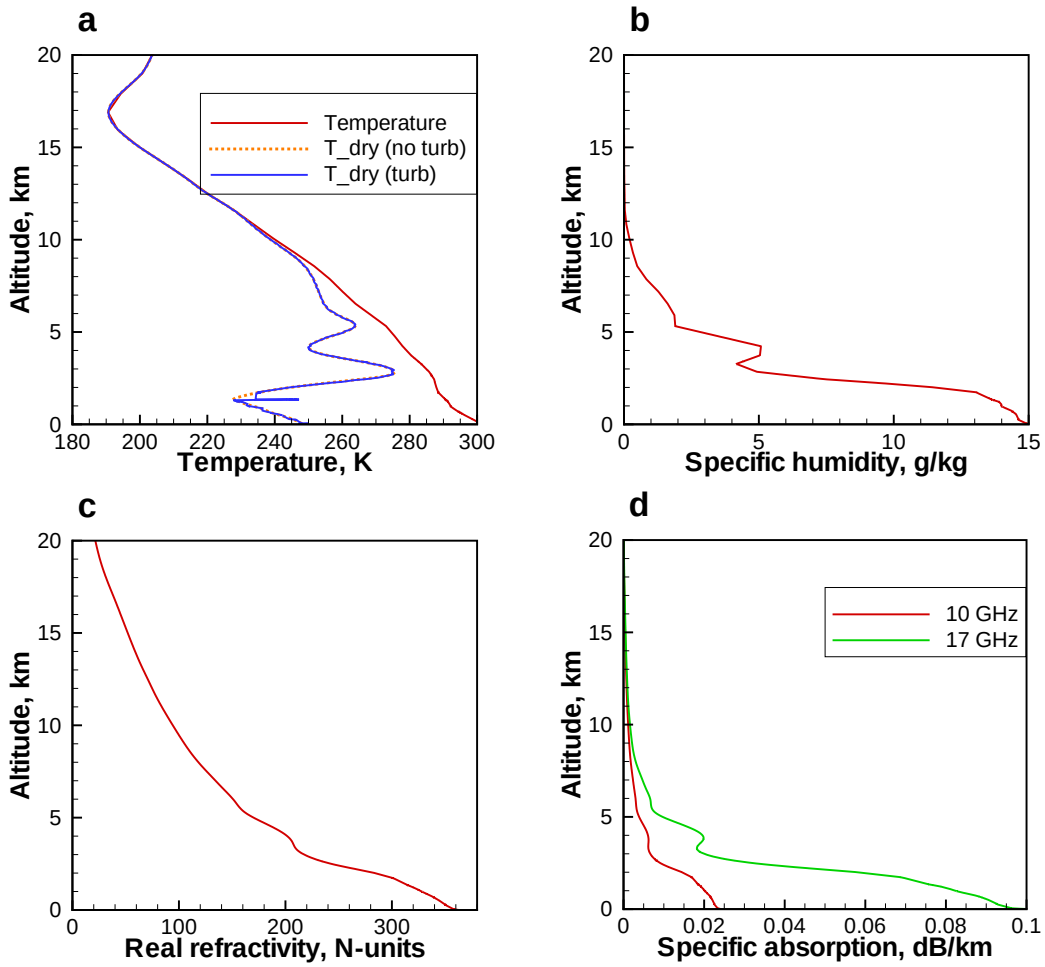

Figure 16: Simulated occultation event 0118, May 29, 2001, UTC 13:12, 10.4°S 140.7°E, ECMWF field with superimposed power turbulence, frequency channels 10 and 17 GHz: (a) temperature T and dry temperature $T_{\rm dry}$ for the regular medium and dry temperature $T_{\rm dry}^{\rm (turb)}$ for the turbulent medium, (b) specific humidity, q, (c) real refractivity, N, and specific absorptions, $(20/\ln 10)kN_I$, for the two frequencies.

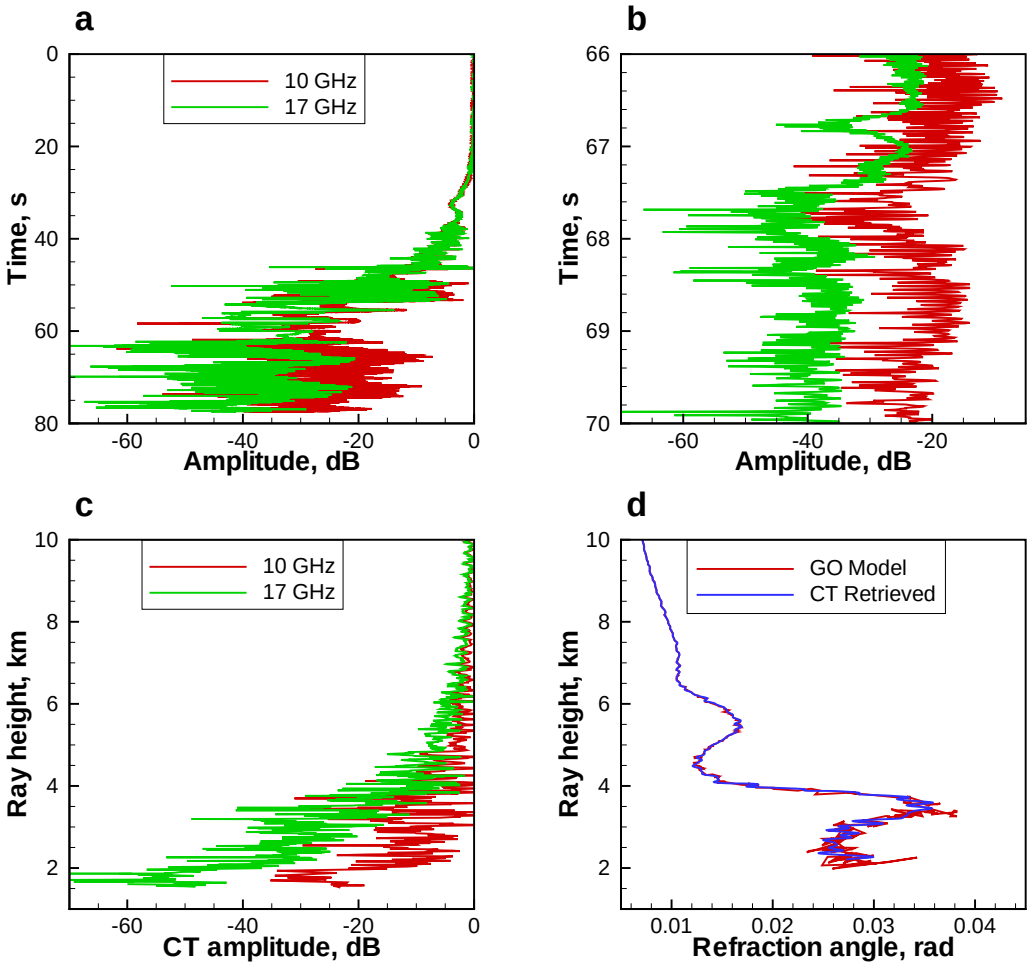

Figure 17: Simulated occultation event 0118, May 29, 2001, UTC 13:12, 10.4°S 140.7°E, ECMWF field with superimposed power turbulence, frequency channels 10 and 17 GHz: (a) amplitudes in the two channels, (b) enlarged fragment of amplitude records in multipath area, (c) CT amplitudes for the two channels, and (d) refraction angles, computed by the GO model and retrieved by the CT method.

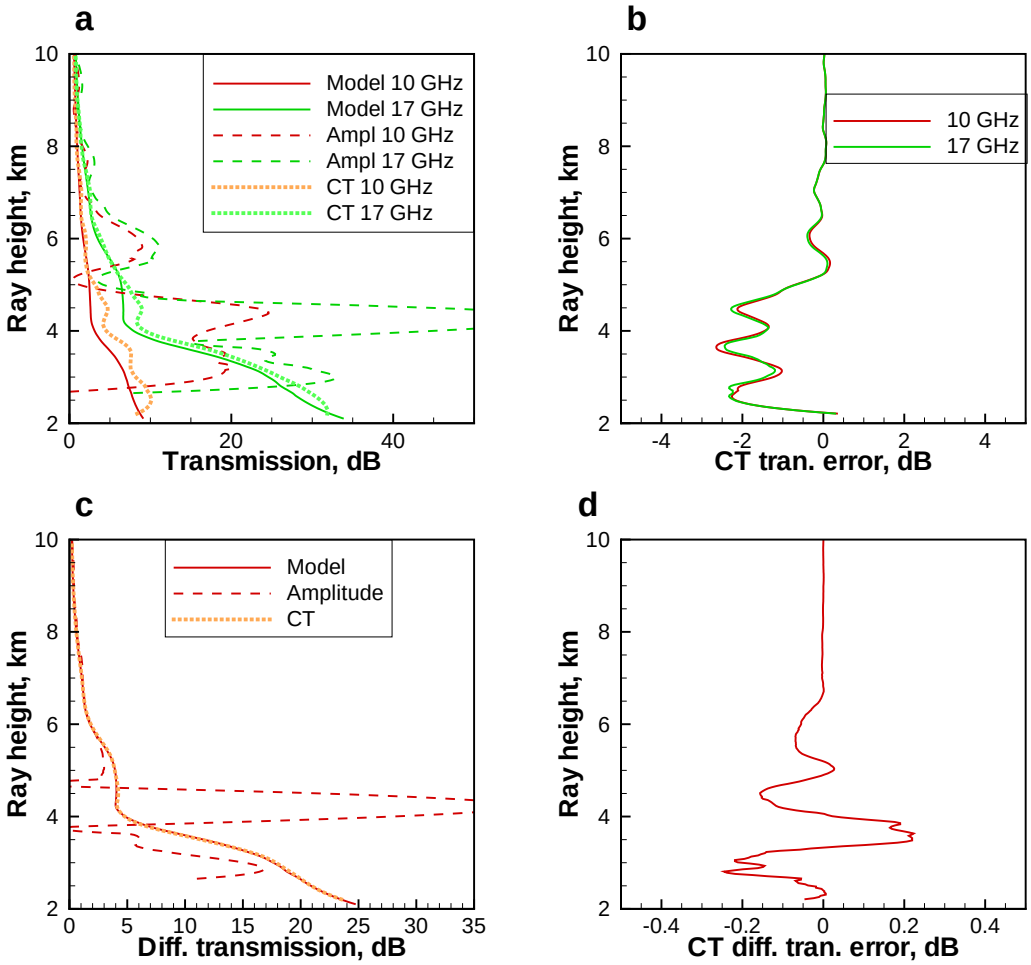

Figure 18: Simulated occultation event 0118, May 29, 2001, UTC 13:12, 10.4°S 140.7°E, ECMWF field with superimposed power turbulence, frequency channels 10 and 17 GHz: (a) transmissions for the two channels, true model, computed from the amplitudes, and computed from the CT amplitudes, (b) errors of the CT transmission, (c) differential transmission, true model, computed from the amplitudes, and computed from the CT amplitudes, and (d) errors of the CT differential transmission.

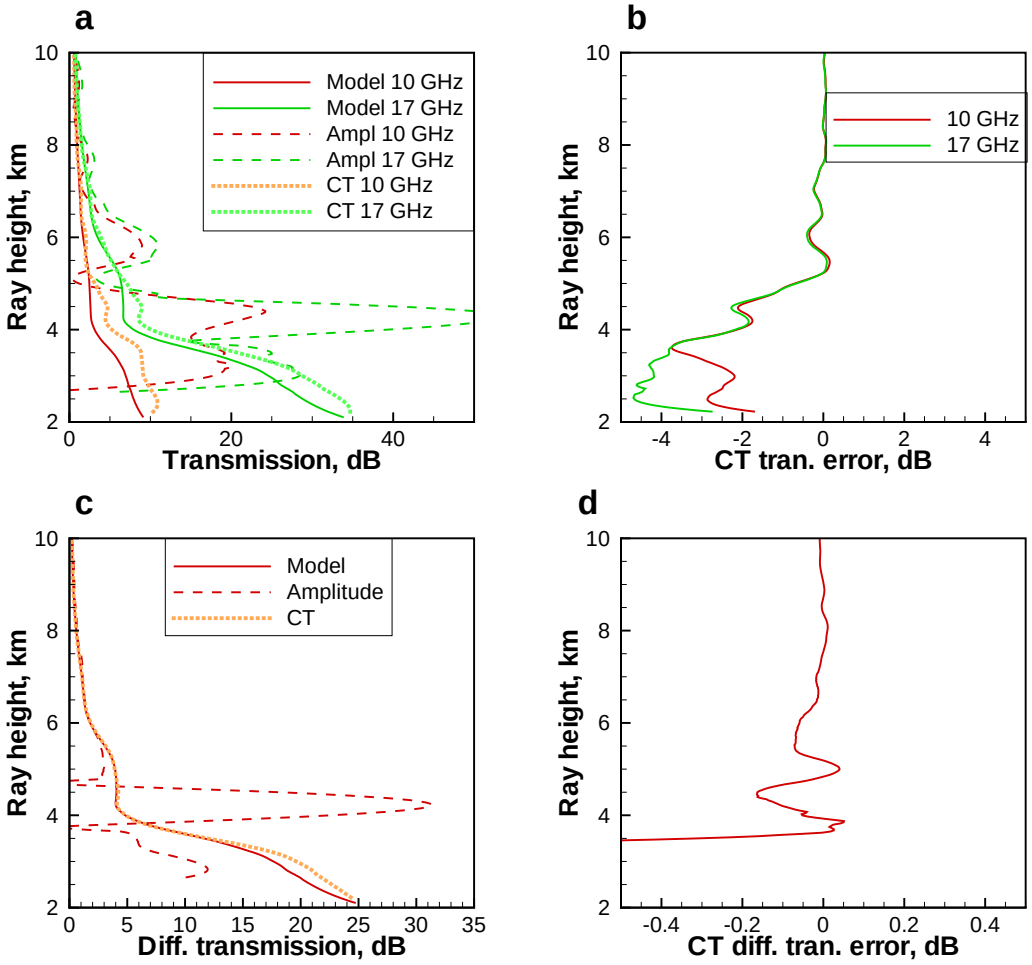

Figure 19: Simulated occultation event 0118, May 29, 2001, UTC 13:12, 10.4°S 140.7°E, ECMWF field with superimposed power turbulence, frequency channels 10 and 17 GHz, with a model of receiver noise 67 dBHz: (a) transmissions for the two channels, true model, computed from the amplitudes, and computed from the CT amplitudes, (b) errors of the CT transmission, (c) differential transmission, true model, computed from the amplitudes, and computed from the CT amplitudes, and (d) errors of the CT differential transmission.

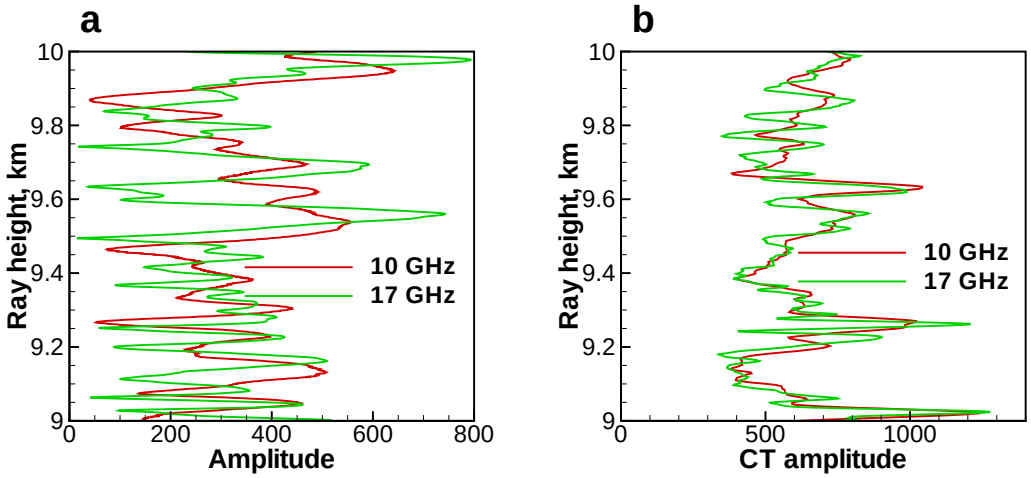

Figure 20: Simulated occultation event 0118, May 29, 2001, UTC 13:12, 10.4°S 140.7°E, ECMWF field with superimposed power turbulence, frequency channels 10 and 17 GHz: (a) measured amplitudes for the two channels, (b) CT amplitudes for the two channels.

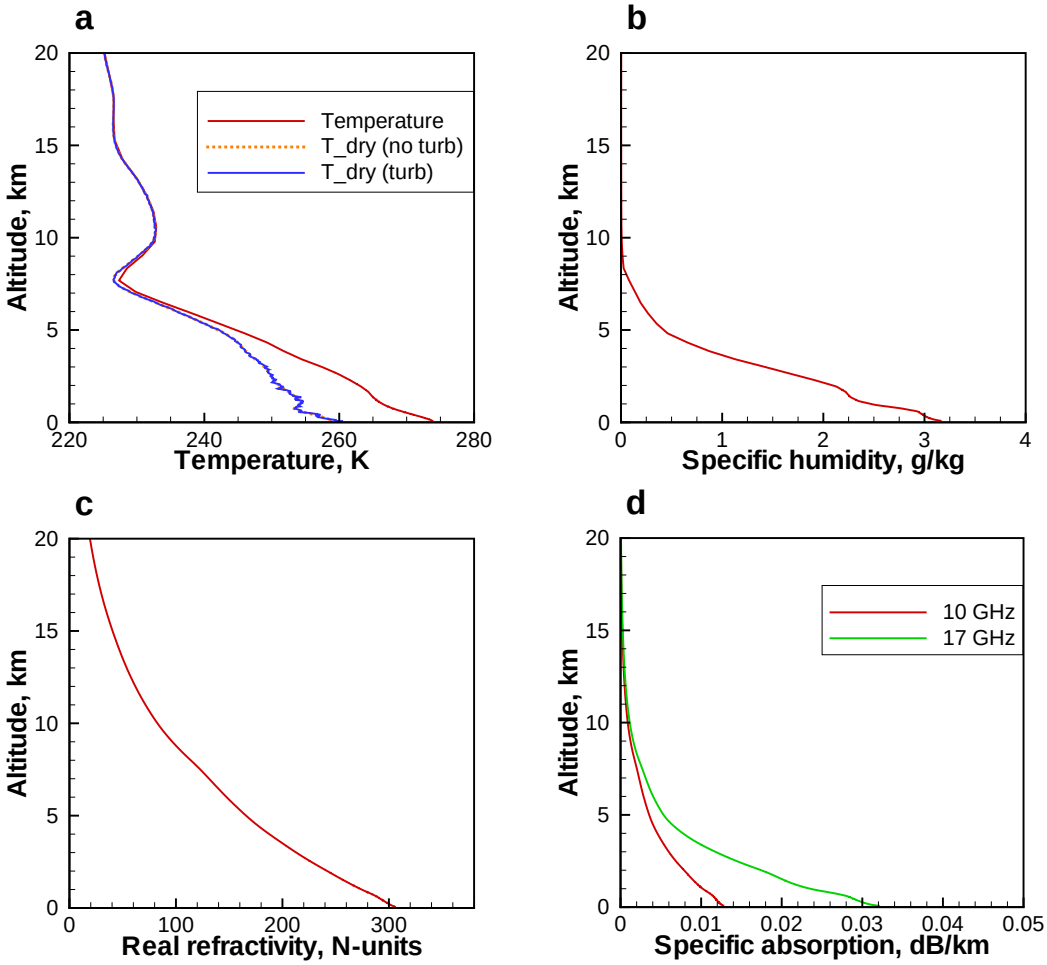

Figure 21: Simulated occultation event 0167, May 29, 2001, UTC 13:12, 67.4°N 54.0°E, ECMWF field with superimposed power turbulence, frequency channels 10 and 17 GHz: (a) temperature T and dry temperature $T_{\rm dry}$ for the regular medium and dry temperature $T_{\rm dry}^{\rm (turb)}$ for the turbulent medium, (b) specific humidity, q, (c) real refractivity, N, and specific absorptions, $(20/\ln 10)kN_I$, for the two frequencies.

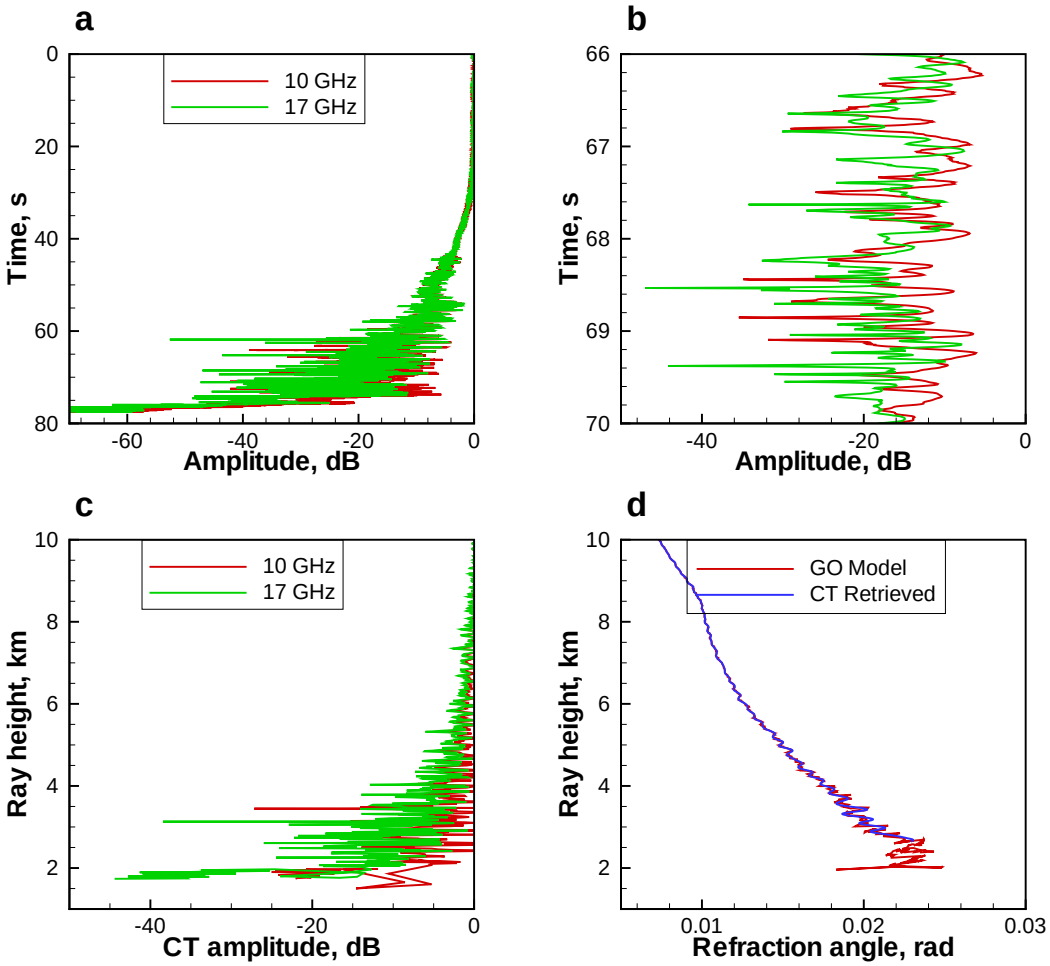

Figure 22: Simulated occultation event 0167, May 29, 2001, UTC 13:12, 67.4°N 54.0°E, ECMWF field with superimposed power turbulence, frequency channels 10 and 17 GHz: (a) amplitudes in the two channels, (b) enlarged fragment of amplitude records in multipath area, (c) CT amplitudes for the two channels, and (d) refraction angles, computed by the GO model and retrieved by the CT method.

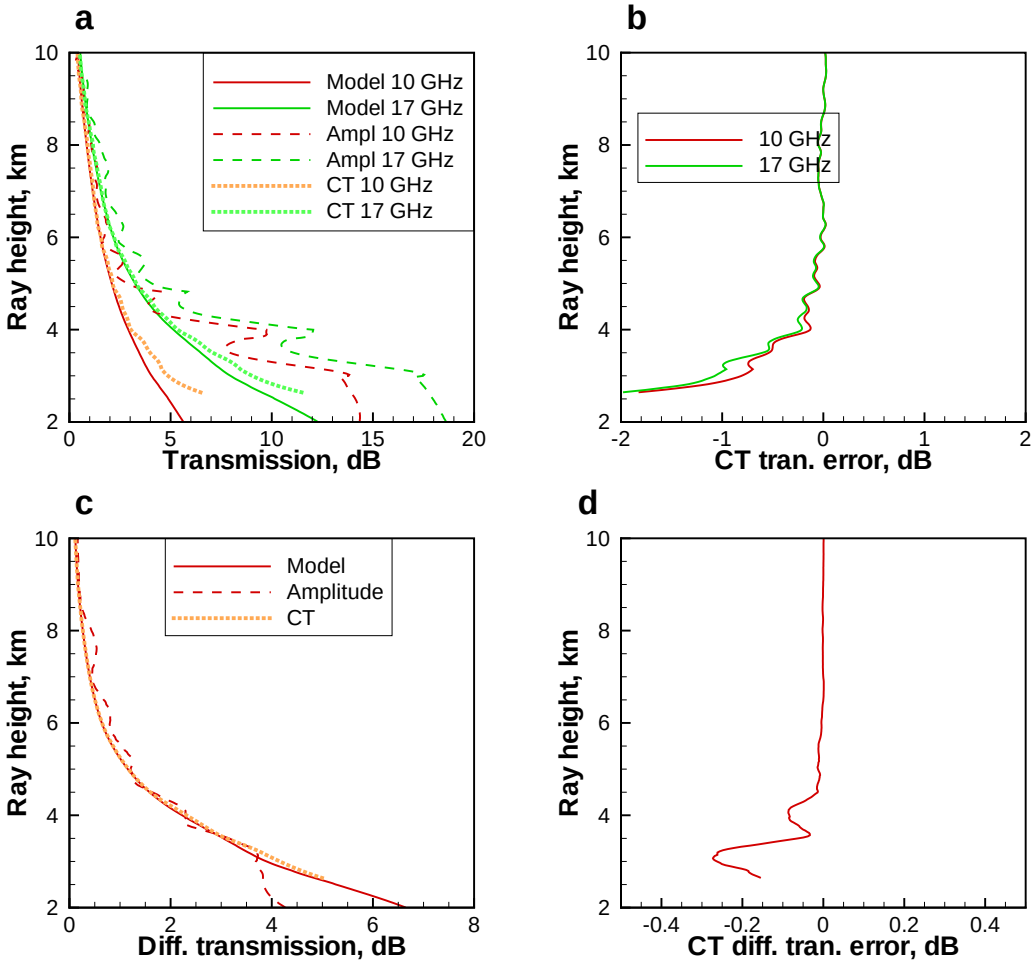

Figure 23: Simulated occultation event 0167, May 29, 2001, UTC 13:12, 67.4°N 54.0°E, ECMWF field with superimposed power turbulence (anisotropy coefficient 20), frequency channels 10 and 17 GHz: (a) transmissions for the two channels, true model, computed from the amplitudes, and computed from the CT amplitudes, (b) errors of the CT transmission, (c) differential transmission, true model, computed from the amplitudes, and computed from the CT amplitudes, and (d) errors of the CT differential transmission.

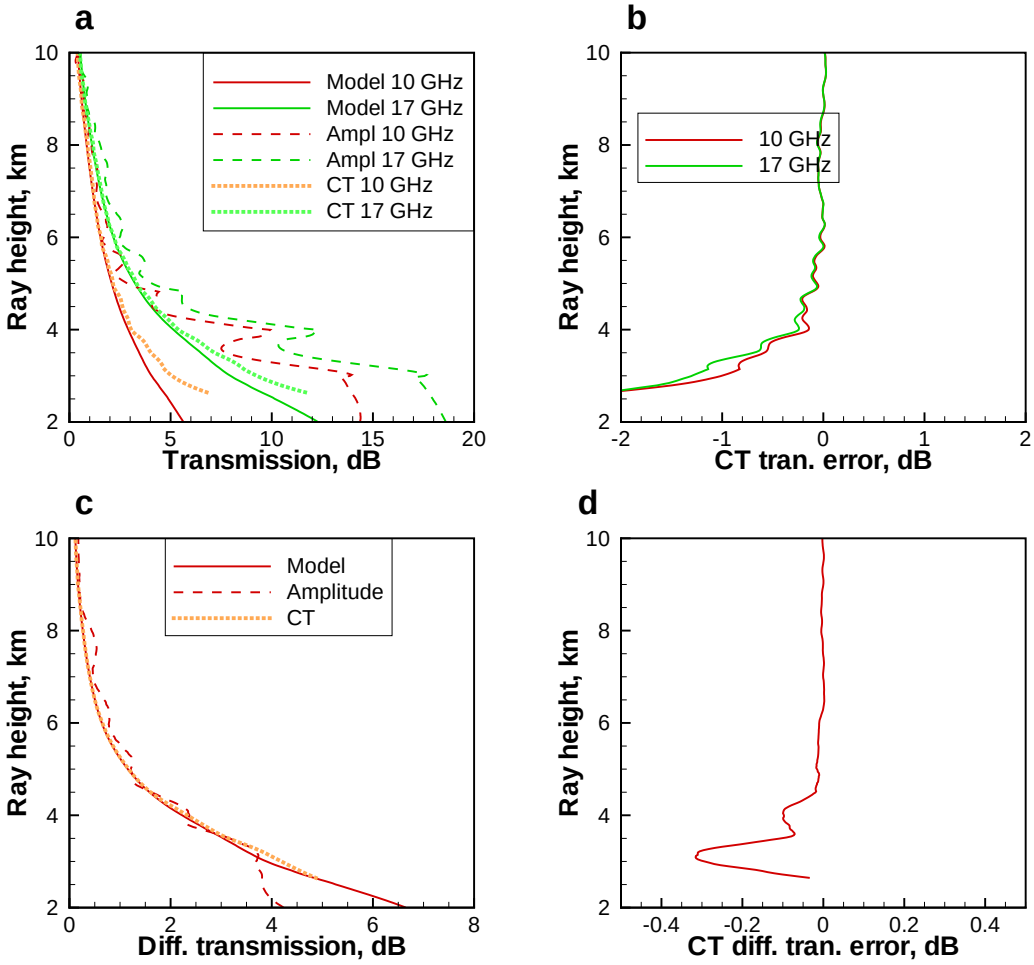

Figure 24: Simulated occultation event 0167, May 29, 2001, UTC 13:12, 67.4°N 54.0°E, ECMWF field with superimposed power turbulence (anisotropy coefficient 20), frequency channels 10 and 17 GHz, with a model of receiver noise 67 dBHz: (a) transmissions for the two channels, true model, computed from the amplitudes, and computed from the CT amplitudes, (b) errors of the CT transmission, (c) differential transmission, true model, computed from the amplitudes, and computed from the CT amplitudes, and (d) errors of the CT differential transmission.

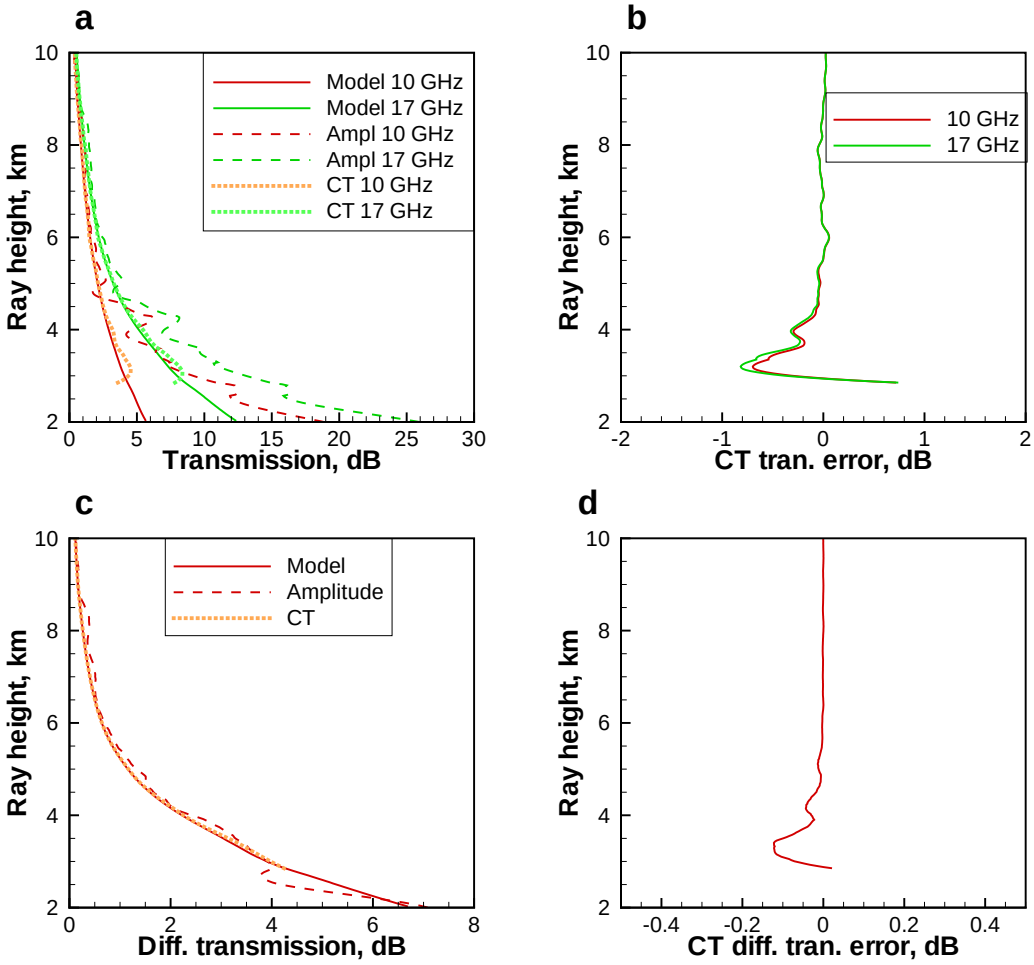

Figure 25: Simulated occultation event 0167, May 29, 2001, UTC 13:12, 67.4°N 54.0°E, ECMWF field with superimposed power turbulence (anisotropy coefficient 10), frequency channels 10 and 17 GHz: (a) transmissions for the two channels, true model, computed from the amplitudes, and computed from the CT amplitudes, (b) errors of the CT transmission, (c) differential transmission, true model, computed from the amplitudes, and computed from the CT amplitudes, and (d) errors of the CT differential transmission.

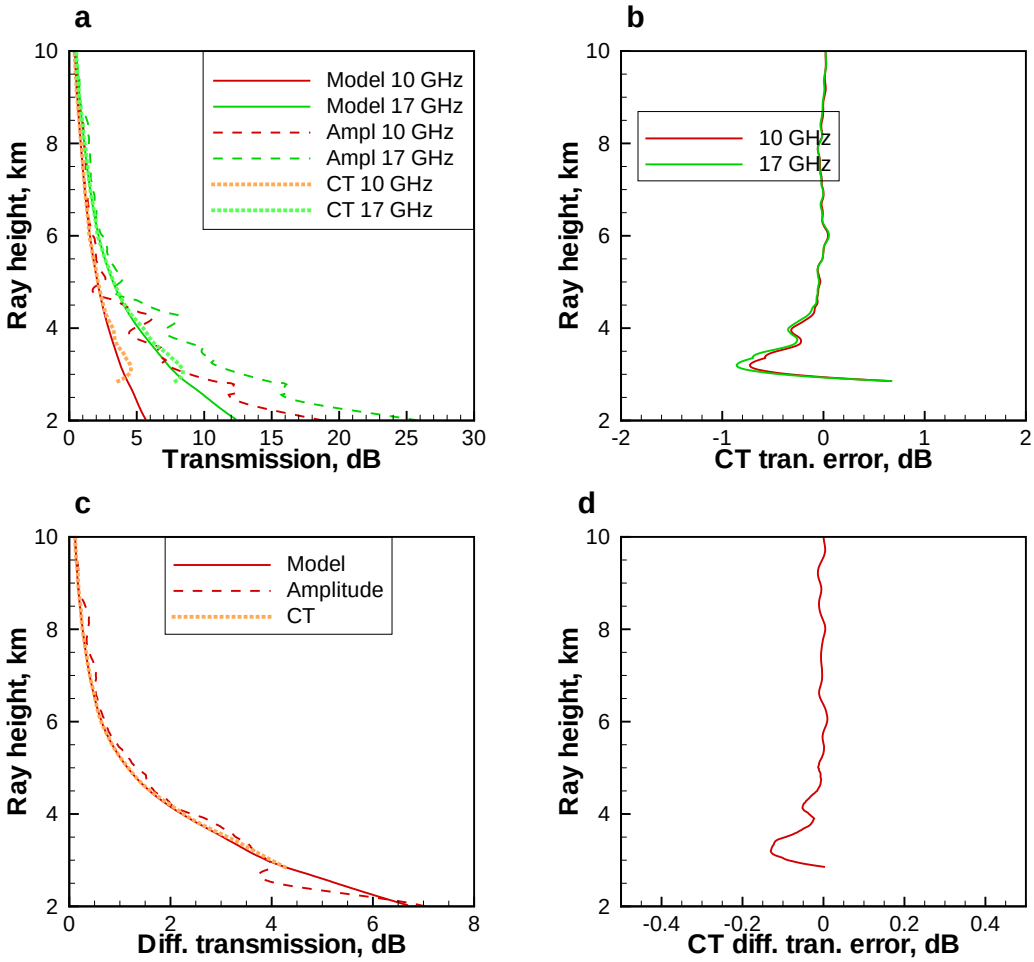

Figure 26: Simulated occultation event 0167, May 29, 2001, UTC 13:12, 67.4°N 54.0°E, ECMWF field with superimposed power turbulence (anisotropy coefficient 10), frequency channels 10 and 17 GHz, with a model of receiver noise 67 dBHz: (a) transmissions for the two channels, true model, computed from the amplitudes, and computed from the CT amplitudes, (b) errors of the CT transmission, (c) differential transmission, true model, computed from the amplitudes, and computed from the CT amplitudes, and (d) errors of the CT differential transmission.